CHAPTER 4

Effect of initial conditions on mean and turbulent flow characteristics of a three-dimensional turbulent wall jet

In the present work, the effect of developing initial conditions on the three-dimensional square wall jet is studied through experimental and numerical methods. The developing initial conditions at the nozzle exit is varied by considering the different lengths of the square nozzles. The length (l) of the square nozzle is varied as l/h=10, 50 and 90, where $h = 20mm$ is the height of the square nozzle. The bulk mean velocity (u_b) at the nozzle exit is $20.3m/s$. The jet exit Reynolds number Re_{jet} based on the height of the square nozzle ($h = 20mm$) and bulk mean velocity (u_b) is $25,000$. The experimental and numerical methods are already described in the previous chapter. The results obtained from experimental and numerical methods are discussed here.

4.1 Experimental results for initial conditions

The effect of different initial velocity conditions on three-dimensional square wall jet is characterized by measuring the mean velocity profile across the jet centerline in lateral and wall-normal directions. The mean velocity profiles are measured from $x/h = 0.2$ to 45 in the three-dimensional wall jet facility with the single probe hotwire anemometer.

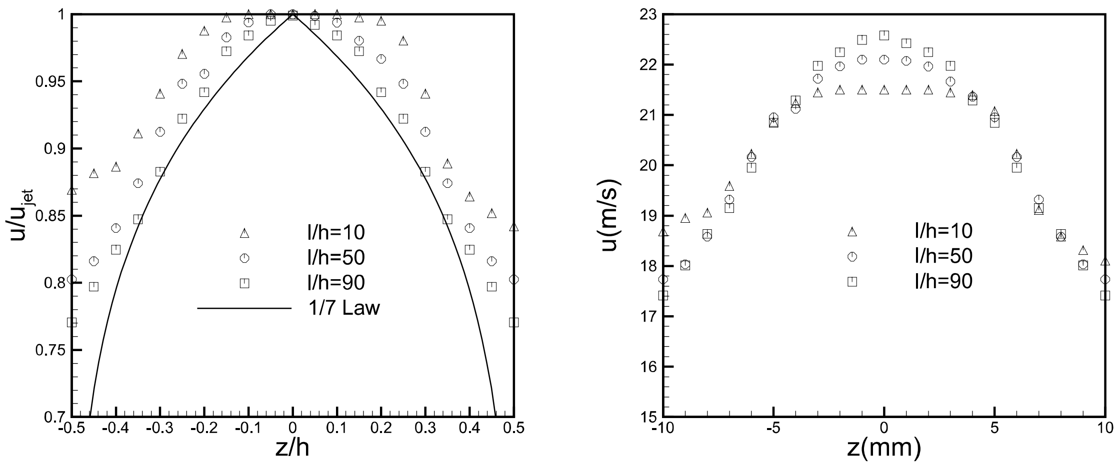

(a) (b)

Figure 4.1: Distribution of mean velocity profile at nozzle exit (a) Non-dimensional jet exit velocity profile, and (b) Dimensional jet exit velocity profile

4.1.1 Inlet jet profile

The effect of varying length of the nozzle on three dimensional turbulent square wall jet is first characterized by jet exit mean velocity profile. The mean velocity profiles are measured along the lateral positions (-0.5≤ z/h≤0.5) of the nozzle exit $\left(x/h = 0.2,\ y/h = 0.5\right)$ for different length of the square nozzles. The bulk mean velocity is kept at 20.3m/s for all the nozzles. The jet exit velocity profiles are normalised by the corresponding jet exit velocity $\left(u_{jet}\right)$ of the different nozzles. The mean velocity profiles adjacent to jet exit in lateral jet centerline plane are shown in figure 4.1a. A dimensional jet exit velocity profile is shown in figure 4.1b. By varying the nozzle length, the jet exit profile is also varied by Antonia and Zhao [60] for a circular free jet. They have considered only a contracted nozzle and a very long nozzle (l/h = 1180) and it was shown that a top hat flat profile is obtained with the contracted nozzle while $1/7^{th}$ law profile is obtained with the long nozzle. In this study, the emphasis is placed on characterising the fluid flow when the condition at the nozzle is developing. To do so, the nozzle length is varied between l/h = 10 to l/h = 90. For a reference value, $1/7^{th}$ law profile is also plotted. It can be seen that our profile is neither fully developed nor top hat.

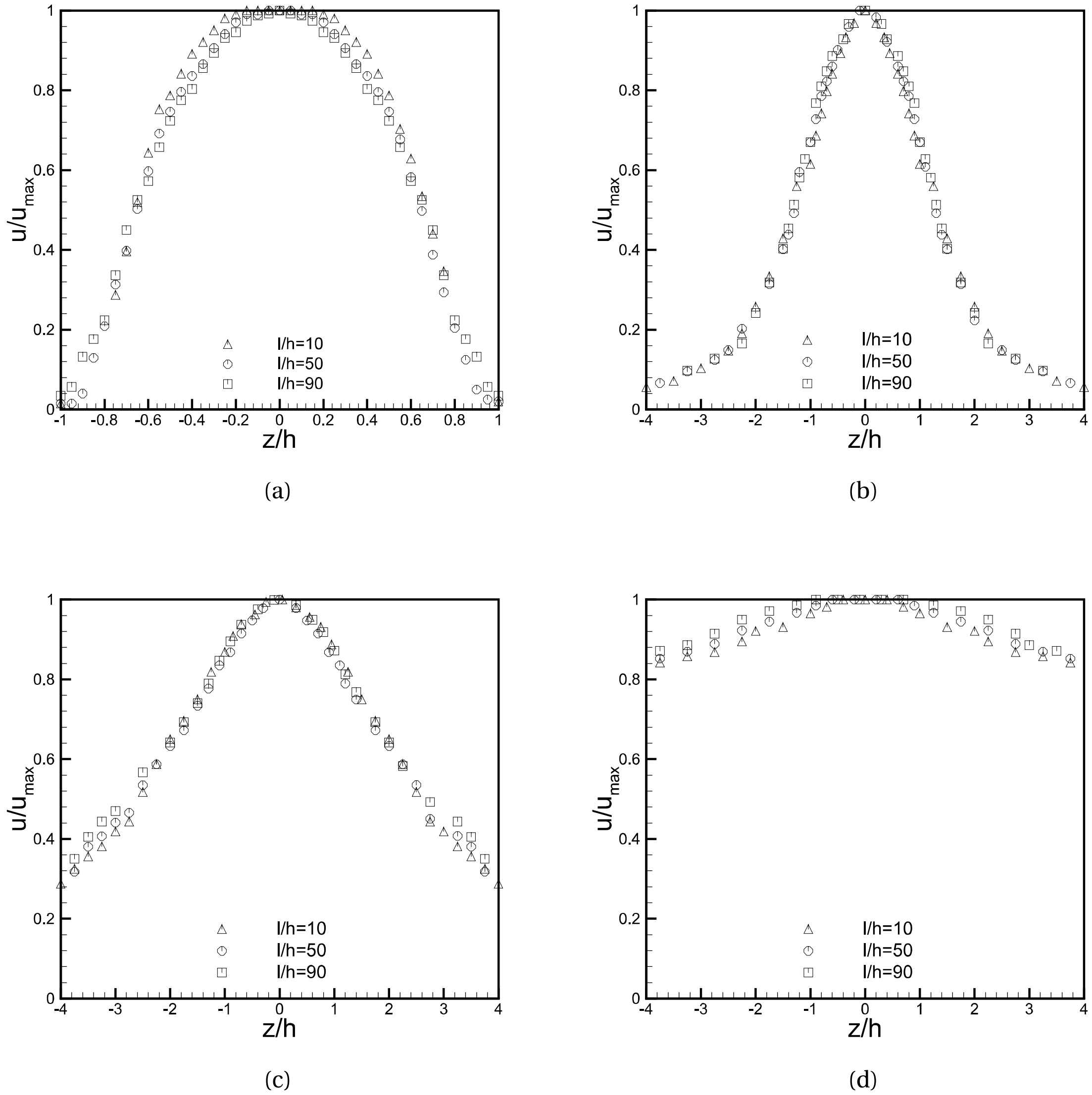

Figure 4.2: Mean streamwise velocity profiles for l/h=10, l/h=50, and l/h=90 at $y/h = 0.5$ and (a) $x/h = 2$, (b) $x/h = 15$, (c) $x/h = 25$ and (d) $x/h = 45$

4.1.2 Velocity variation in the lateral and wall-normal planes

The development of the three dimensional turbulent square wall jet is studied by mean velocity profile distribution across the jet centerline. The mean velocity is normalised by the local maximum velocity (u_{max}), whereas its location is normalised by the height (h) of the square jet. The lateral velocity profiles issuing from different nozzle lengths ($l/h = 10$, 50, and 90) are shown in figure 4.2, in the range of 2≤ x/h ≤45. From the figure, it is evident that the growth occurs earlier for the nozzle length l/h=10, due to the uniform inlet profile compared to nozzle length $l/h = 50$ and $l/h = 90$. In the near field region ($0 \leq x/h \leq 25$), the rate of velocity decay and spread are dependent upon the nozzle length. This may be attributed to the different momentum at the jet exit due to the different shape of initial velocity profiles. The different shape of the initial velocity profiles at the jet exit enable the momentum loss to the ambient. In the developed region ($x/h \geq 25$), the velocity profile for all the nozzles almost collapsed into a single profile showing a very little effect of the jet initial velocity profiles. The effect of sidewall on the velocity profile can be noticed, which shows a non-zero velocity near the wall. It is seen that the jet strikes the sidewall near $x/h = 15$, reflecting in the growth of turbulence near the sidewall. This growth becomes more pronounced while moving further downstream (please see figures 4.2d). As a result, the velocity profile becomes almost flat.

The wall-normal mean velocity profile is plotted for the different nozzle lengths (l/h) at different downstream locations (x/h) in figure 4.3. The measurements are taken in the vertical plane of $z/h = 0.0$ at different downstream locations in the range x/h= 2 to 45. The effect of nozzle lengths also appears in the wall-normal velocity distribution profiles up-to $x/h \leq 25$. As the fluid exits from the nozzle, the jet tries to expand across the jet centerline. The upper shear layer of the jet expands in the ambient, but lower shear layer of the jet is restricted by the horizontal wall. Therefore, the expansion of the flow stream is discontinued below the jet centerline and mean volume shifts in between the jet centerline and bottom wall. The behaviour of the jet for different initial conditions can be seen in figure 4.3. The local maximum mean velocity is observed below the jet centerline. It is noted here that the velocity very close to the wall surface is not captured because of the limitation of the hot wire anemometer.

4.1.3 Variation of jet half-width

The effect of initial condition and sidewall effect on the spread behaviour, the jet half-width in wall-normal and lateral direction are evaluated. The jet half-width in the wall-normal and lateral directions is defined as the location of mean velocity where $u(x, y, z) = u_{max}/2$. The variation of $y_{1/2}/h$ in the wall-normal direction for different nozzle lengths is shown in figure 4.4a. From the figure, it is observed that the jet half-width is reduced near the nozzle exit for all the cases. But, after this, the jet half-width varies linearly with x/h. The jet half-width ($y_{1/2}/h$) in the wall-normal direction is higher for $l/h = 10$ nozzle, in the near field, as compared to the nozzles $l/h = 50$ and $l/h = 90$ (see figure 4.4b). This is due to the higher diffusion of jet fluid into the ambient for the nozzle $l/h = 10$. However, this trend becomes entirely opposite after $x/h > 10$. This is possible because u_{max} is higher for $l/h = 10$ nozzle which increases the entrainment from the surrounding. As a result,

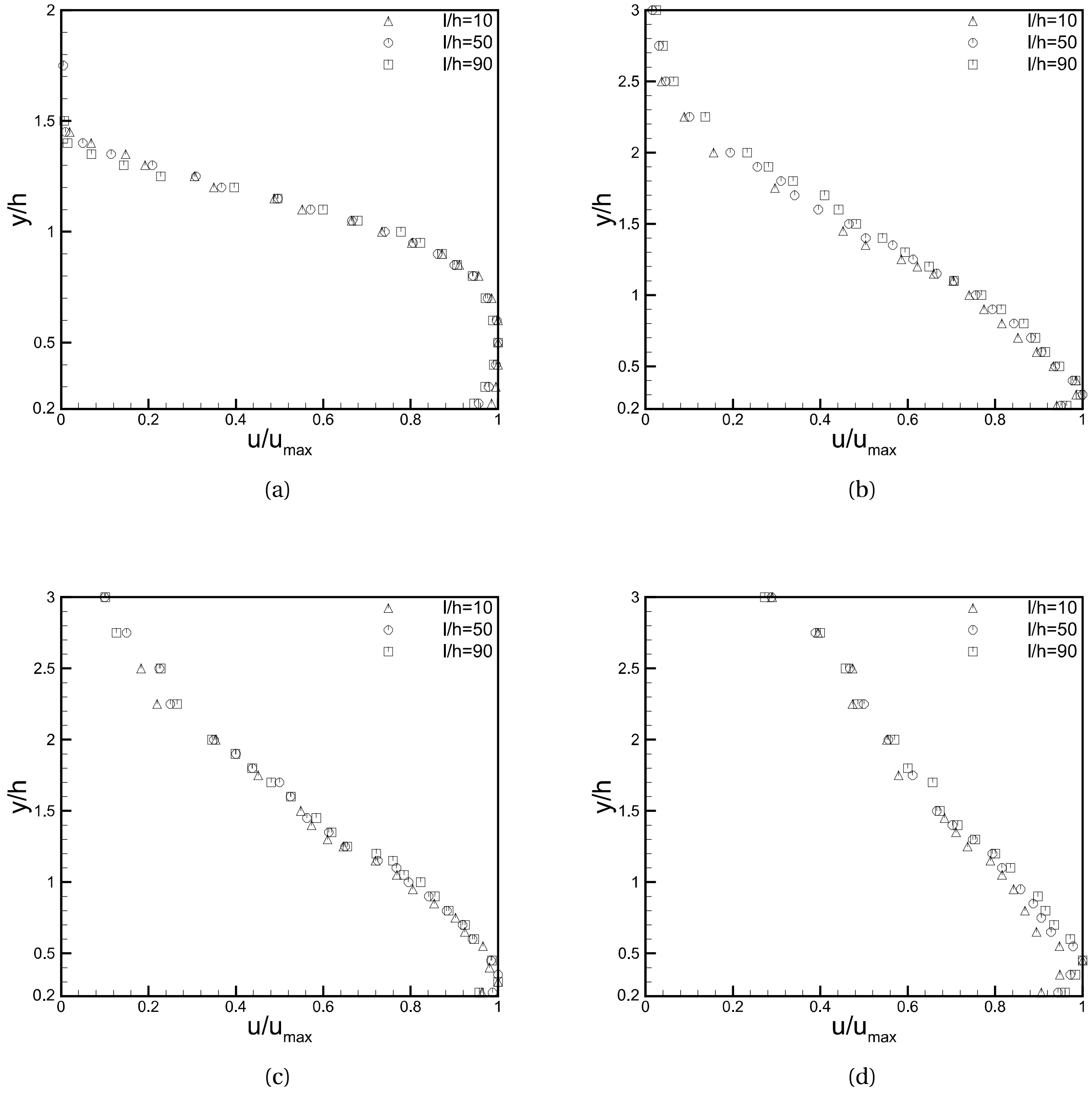

Figure 4.3: Wall-normal mean velocity profiles for l/h=10, l/h=50,and l/h=90 at y/h=0.5 and (a) x/h=2, (b) x/h=15, (c) x/h=25 and (d) x/h=45

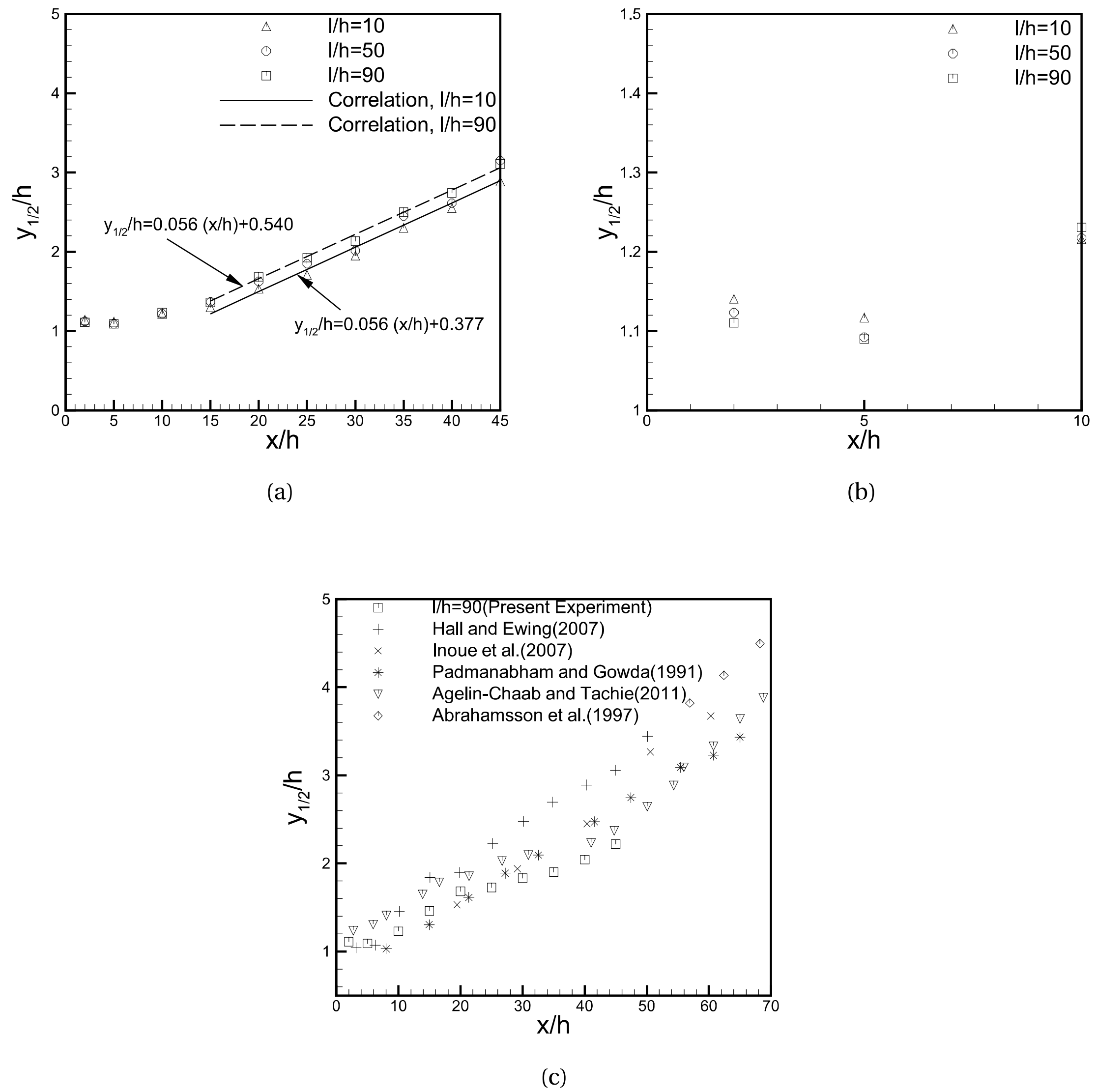

Figure 4.4: Jet half-width (a) $y_{1/2}/h\,Vs\;x/h$ for nozzle l/h=10, 50, and 90 (b) Zoom view of jet half-width in near field ($x/h \leq 10$) ((c) Comparison of $y_{1/2}/h\,Vs\;x/h$ for l/h=90 with Hall and Ewing [9], Inoue et al. [10], Padmanabham and Gowda [2], Agelin-Chaab and Tachie [11] and Abrahamsson et al.[12]

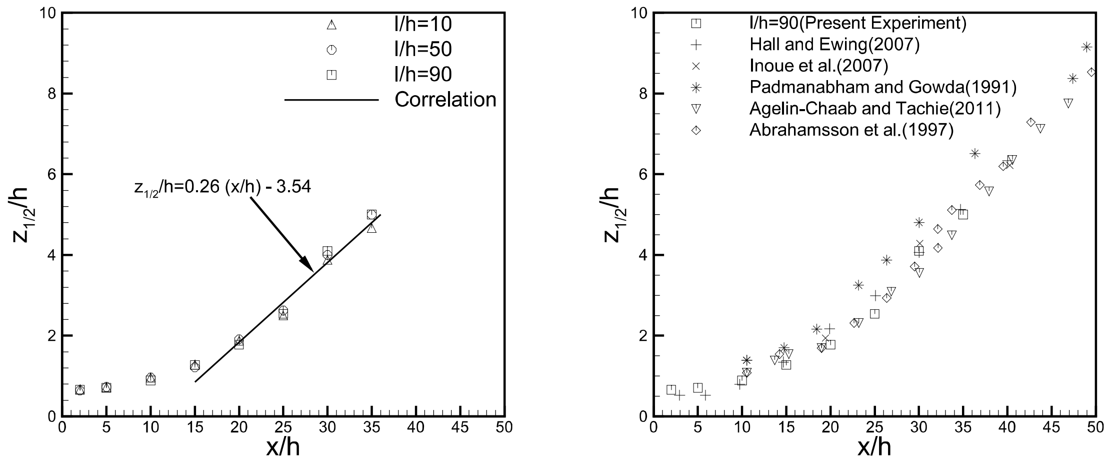

(a) (b)

Figure 4.5: Jet half-width (a) $z_{1/2}/h$ Vs x/h for nozzle l/h=10, 50, and 90 (b) Comparison of $z_{1/2}/h$ Vs x/h for $l/h = 90$ with Hall and Ewing [9] and Inoue et al. [10], Padmanabham and Gowda [2], Agelin-Chaab and Tachie [11] and Abrahamsson et al. [12]

the fluid is pushed more towards the lower wall which ultimately decreases $y_{1/2}/h$. But, the spread rate is noticed to be independent of the nozzle length (l/h). A comparison has been made for the jet half-width in the wall-normal direction of $l/h = 90$ nozzle with Hall and Ewing [9] as shown in figure 4.4c. The jet half-width of Hall and Ewing [9] is higher as compared to the present result. This difference may be attributed to the presence of sidewall which restricts the entrainment from the surroundings. The jets with sidewall have less spread rate as compared to the jets without sidewall, but the growth of jet half-width is similar to the previously reported result [9]. This may be due to the less interaction of the ambient fluid with the jet stream. This needs further investigation on the effect of sidewall on three-dimensional turbulent wall jet. A linear equation $\left(\frac{y_{1/2}}{h}\right) \sim a\left(\frac{x}{h}\right) + b$ has been fitted in the range of $15 \leq x/h \leq 45$, for the different nozzle lengths as shown in figure 4.4a. The value of R^2 for the experimental and correlated data is approximately 97.92.

The variation of jet half-width in the lateral direction is shown in figure 4.5a. From the figure, it is observed that after $x/h \geq 15$, the jet half-width varies linearly along the downstream locations and the spread rate becomes independent of the nozzle length (l/h). The growth of the jet half-width in the lateral direction is compared with the results of Hall and Ewing [9], Inoue et al. [10], Padmanabham and Gowda [2], Agelin-Chaab and Tachie [11], and Abrahamsson et al. [12], as shown in figure 4.5b. The collapse of the present result of

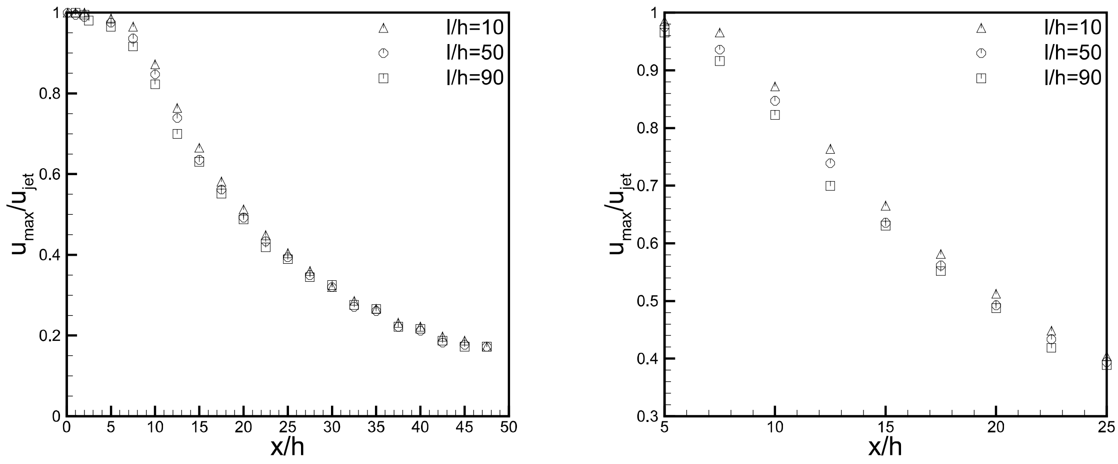

(a) (b)

Figure 4.6: (a) Decay of jet exit velocity (b) Zoom view of jet exit velocity

nozzle $l/h = 90$ with the existing data on a single line suggests that the nozzle length does not affect the spread rate in the lateral direction and the sidewall as well. A linear equation $\left(\frac{z_{1/2}}{h}\right) \sim a\left(\frac{x}{h}\right) + b$ has been fitted with the experimental data in the range of $15 \leq x/h \leq 35$ for the different nozzle lengths ($l/h = 10-90$). The curve is fitted with a value of R^2 more than 97.51%.

From the present data set, the spread rate in wall-normal direction$\left(\frac{d(y_{1/2}/h)}{dx/h}\right)$ is found to be 0.056. This value is within the accepted range of literature data reported by different authors. The spread rate in the lateral direction$\left(\frac{d(z_{1/2}/h)}{dx/h}\right)$ for $l/h = 10-90$ is found to be 0.26. Also, it is interesting to note that the spread rate in the lateral direction is independent of the nozzle length. The ratio of $\left(\frac{d(z_{1/2}/h)}{dx/h}\right)/\left(\frac{d(y_{1/2}/h)}{dx/h}\right)$ is found to be 4.64, which is within the range of widely available literature data. These results show that variation of jet half-width is consistent with the previously reported data.

4.1.4 Decay of maximum mean velocity

The effect of different initial conditions is studied by the decay of maximum mean velocity (u_{max}) in the downstream direction from the nozzle exit. It is expected that the normalized maximum mean velocity profile continuously decreases due to the momentum dissipation and spread of the mean flow stream for all the nozzles, as shown in figure 4.6. The maximum mean velocity and the downstream location is normalized with the jet exit velocity (u_{jet}) and the height of the square nozzle (h) respectively for each case. It is seen in the near field region ($x/h < 5$), the maximum mean velocity decays with a very slow rate up-to some distance from the nozzle exit. This distance belongs to the potential core and it is found at $x/h = 4, 3$ and 2 for the nozzle length l/h= 10, 50 and 90 respectively. This may be due to the available velocity gradient at the nozzle exit from the jet centerline. After the consumption of the potential core, the decay rate of maximum mean velocity is increased in the region of ($5 \leq x/h \leq 25$) for all the cases due to the mixing of the different shear layers. In this region (see figure 4.6b), the decay rate along the downstream is seen higher for the nozzle lengthl/h=10. The correlated curve for $l/h = 10$ is described in this region as $u_{max}/u_{jet} \sim (x/h)^{-0.73}$. The correlated curve for $l/h = 50$ and $l/h = 90$ shows relatively lower decay rate than $l/h = 10$, and it is found as $u_{max}/u_{jet} \sim (x/h)^{-0.72}$ and $u_{max}/u_{jet} \sim (x/h)^{-0.71}$ for $l/h = 50$ and $l/h = 90$ respectively. In the fully developed region ($25 \leq x/h \leq 45$), the decay of maximum mean velocity becomes independent of the nozzle length (l/h) and location of the sidewall. In this region, the velocity decays as per the power law:

$$\frac{u_{max}}{u_{jet}} = a\left(\frac{x}{h}\right)^{-n} \tag{4.1}$$

The values of a and n are found out by the least square method, where n is known as the decay rate of the u_{max}. The combined average decay rate for different initial conditions in fully developed region is found to be 1.08 with $R^2 = 0.99$. Further, for the comparison of the decay of maximum mean velocity for $l/h = 90$, the results of Hall and Ewing [9], Agelin-Chaab and Tachie [11], Kwakye et al. [13], and Kumar and Das [14] are also added as shown in figure 4.7. Hall and Ewing[9] and Agelin-Chaab and Tachie [11] show higher decay than the present case. This is due to the presence of sidewall in the present experiment. Kwakye et al. [13] obtained the lower rate of decay of maximum mean velocity because of the shape of the nozzle. They [13] considered a strip shape of the nozzle which reduced the decay in the lateral direction. The lower rate of decay is also obtained by Kumar and Das [14] for the two dimensional case, in which the decay in lateral direction is negligible. It is found that $l/h = 90$ shows higher local maximum mean velocity due to the presence of the sidewall closer to the nozzle which pushes the fluid towards the centerline of the nozzle. That leads to a rise in the local maximum mean velocity. The decay rate reported by other authors is listed in the table 4.1.

4.1.5 Local Reynolds number variation

The variation of the local Reynolds number (Re_x) for different nozzle lengths (l/h) is shown in figure 4.8. The local Reynolds number is defined as $Re_x = (u_{max} \times y_{1/2})/\nu$. The local

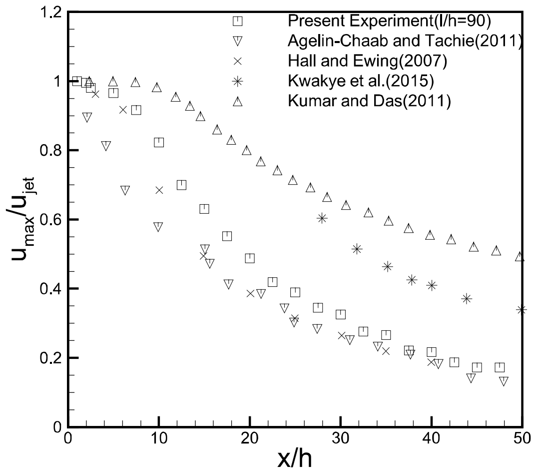

Figure 4.7: Maximum mean velocity comparison with Agelin-Chaab and Tachie [11], Kwakye et al. [13], Hall and Ewing [9], Kumar and Das [14]

Table 4.1: Decay of maximum mean velocity

Authors	Reynolds number	Nozzle geometry	Decay rate (n)
Agelin-Chaab and Tachie [11]	5000, 10000, 20000	Circular	1.15
Kwakye et al. [13]	12000	Rectangular	0.996
Fujisawa and Shirai [138]	60,000	Square	1.12
Hall and Ewing($l/h = 96$) [9]	98,600	Rectangular (A.R.=1)	1.144
Present ($l/h = 10-90$)	25000	Square	1.08±0.02
Kumar and Das [14]	15000	2D	0.2

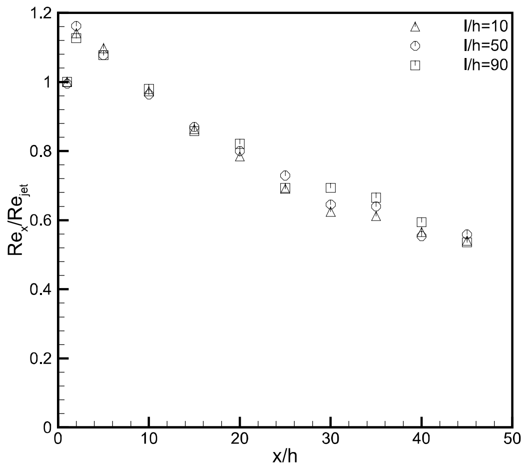

Figure 4.8: Development of the local Reynolds number for different initial conditions (l/h=10, 50 and 90)

Reynolds number (Re_x) for each initial condition of the nozzle decreases as the flow develops in the downstream directions. As the flow develops in the downstream directions, the jet exit Reynolds number (Re_{jet}) reaches approximately 56% for nozzle l/h = 10 at x/h = 40. The local Reynolds number (Re_x) at the same location for the nozzle l/h = 50 and l/h = 90 is approximately $0.02Re_{jet}$ and $0.03Re_{jet}$ larger than the nozzle l/h = 10 respectively. This happens because ($y_{1/2}/h$) increases with l/h at this location.

4.1.6 Self-similar behaviour

The effect of different lengths of nozzle l/h = 10, 50, and 90 on the self-similar behaviour in the wall-normal plane is shown in figure 4.9. To get the self-similar behaviour for the three dimensional turbulent square wall jet, streamwise velocity (u) is normalized with the local maximum mean velocity (u_{max}) and the wall-normal location (y) is normalized by the wall-normal jet half-width ($y_{1/2}$), as suggested by Wygnanski et al. [32]. It is observed that the self similar behaviour is obtained at x/h = 20 for l/h = 10 nozzle, but for all other nozzles, it is a little delayed towards the downstream direction(x/h = 25). The reason behind this is the different shapes of initial jet profile for the different nozzle lengths. It is observed from the figure 4.1 that the inlet velocity profile is flat for l/h = 10 as compared to the nozzles l/h = 50 and l/h = 90. This leads to more entrainment of mass from the ambient. So, the development of the flow for l/h = 10 nozzle starts early as compared to the other nozzles (l/h = 50 and 90). The self-similar profile for l/h = 90 nozzle is compared with the results of Hall and Ewing [9] and Rajaratanam and Subramanya [15] for the different downstream locations as shown in figure 4.10. Figure 4.10 shows a good agreement between the present experimental result and the results found in the literature.

Similar to the mean velocity in wall-normal direction, the self similarity profile for the square jet is also tested in the lateral plane for the different downstream locations. The mean velocity (u) in the lateral plane is also normalized with the local maximum mean velocity as (u_{max}) and the location of velocity in the lateral direction (z) is normalized with the corresponding lateral jet half-width ($z_{1/2}$). The similarity profile for different nozzle lengths, i.e. l/h = 10, 50, and 90 is shown in figure 4.11. It is observed that all the profiles collapse into a single curve. This indicates that initial conditions of the nozzle does not have any significant effect in the lateral direction. The similarity profile of Hall and Ewing [9] is also included for the comparison with the present data, as shown in figure 4.12. A good agreement of the results can be noticed in this figure.

The delay in self similar profiles in wall-normal direction as compared to the lateral direction suggests that more turbulence vortices are present in the upper shear layer as compared to the lateral shear layer. The agreement of the present similarity results with

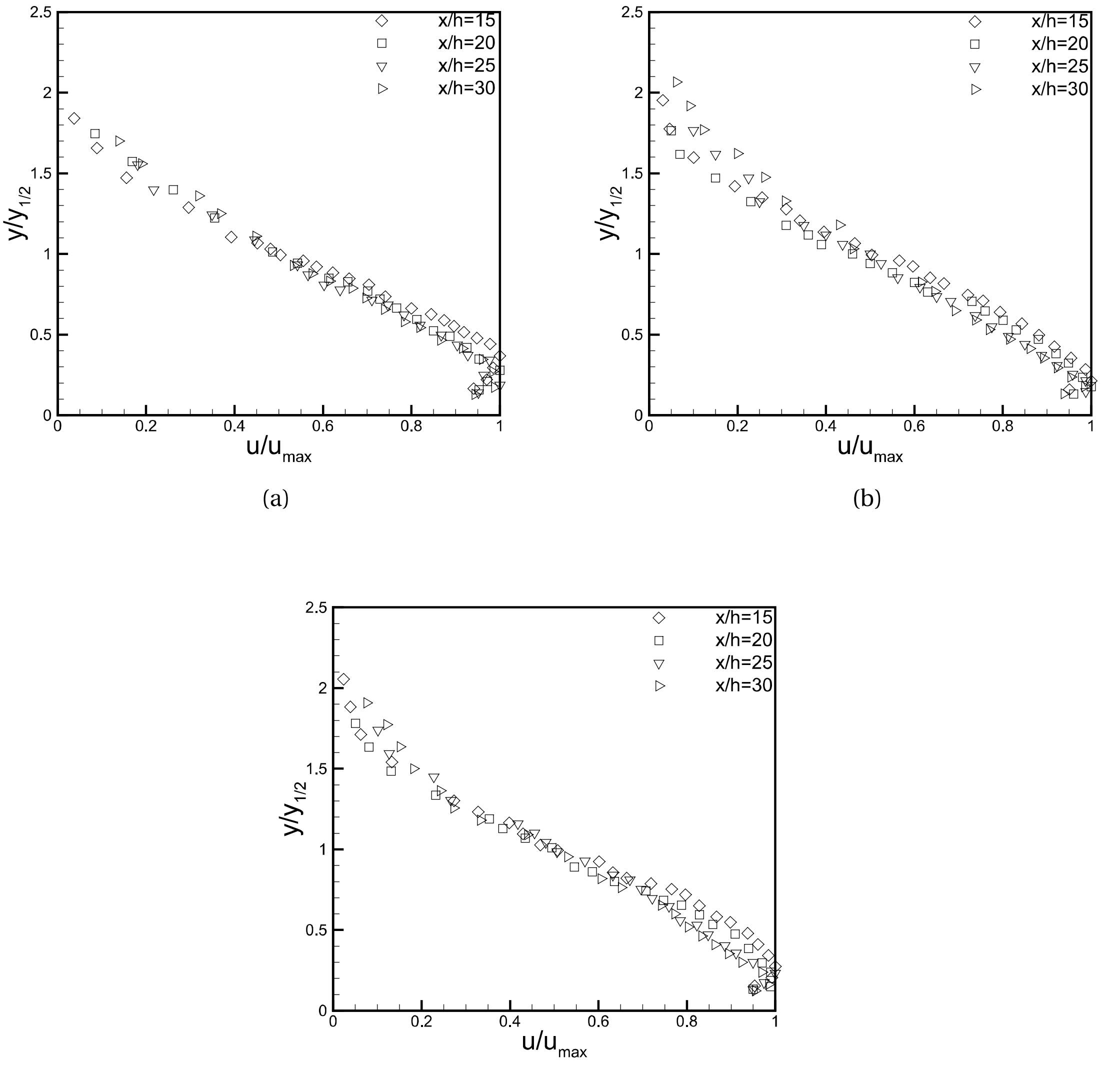

Figure 4.9: Self-similar profile for nozzle (a) l/h=10, (b) l/h=50 and (c) l/h=90

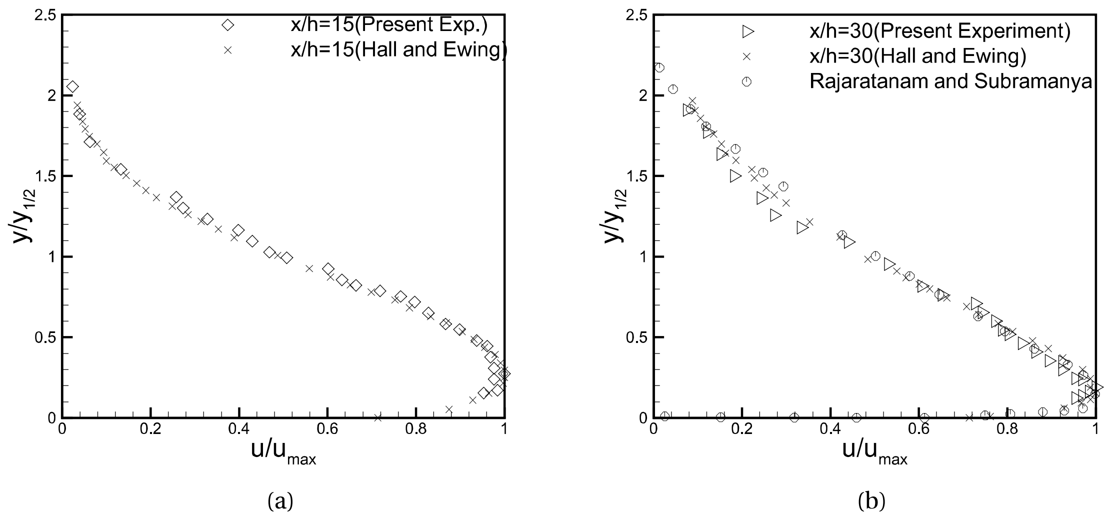

Figure 4.10: Self-similar profile comparison at (a) x/h = 15 and (b) x/h = 30 for nozzle l/h=90 with Hall and Ewing [9] and Rajaratanam and Subramanya [15]

the different authors' results in the fully developed region (in lateral and wall-normal directions) shows that self similar profiles are independent of the initial conditions of the nozzle.

4.2 Numerical results for the effect of initial conditions

The effect of developing initial velocity profiles in a three-dimensional square wall jet has been studied for a Reynolds number of 25,000 through low Reynolds number turbulence modelling, as suggested by Yang and Shih [47] and Launder and Sharma [48]. The initial conditions are varied by changing the nozzle length (l/h = 10, 50 and 90). The flow domain ($50h \times 10h \times 20h$, where h is the nozzle height) for numerical simulation is taken similar to the experimental test section.

4.2.1 Decay of maximum streamwise velocity

The decay of maximum streamwise velocity (u_{max}) depends on the initial conditions like nozzle shape, inlet velocity profiles, and the Reynolds numbers. The decay of u_{max} in the vertical jet centerline plane along the downstream direction from the nozzle exit can be divided into three different regions [2, 9]. In the first region ($0 \le x/h \le 5$), the velocity of the flow field is equal to the jet exit velocity. This region is also known as the potential

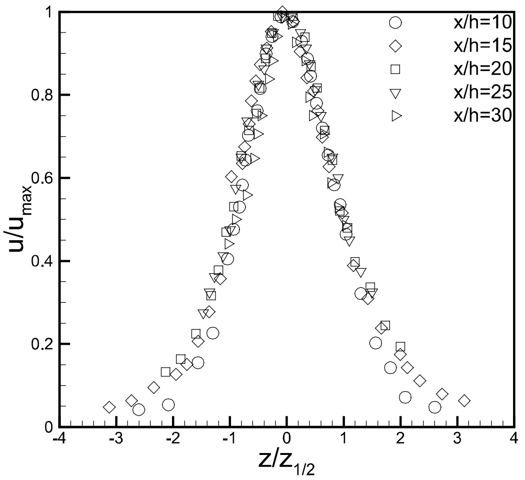

(a)

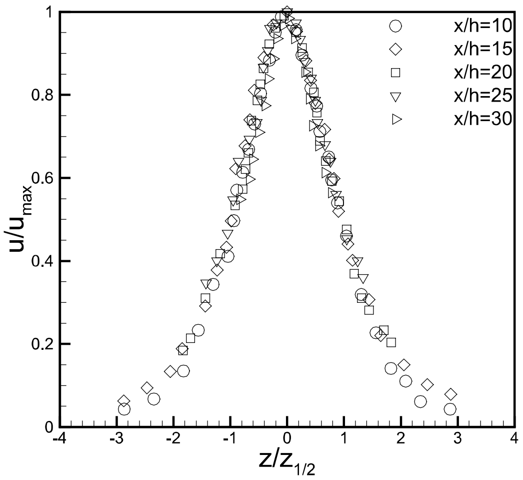

(b)

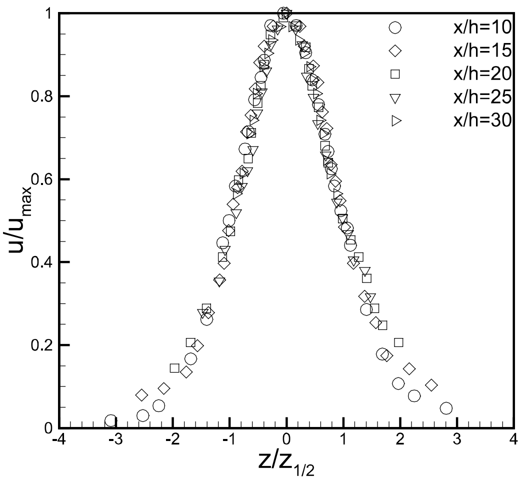

(c)

Figure 4.11: Self-similar profile for Nozzle (a) l/h=10, (b) l/h=50 and (c) l/h=90

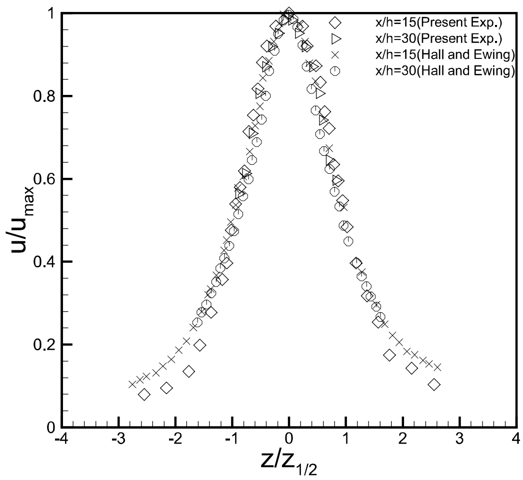

Figure 4.12: Self-similar profile comparison for Nozzle l/h=90 with Hall and Ewing [9]

Table 4.2: Length of potential core at different initial conditions

Initial condition	Length of potential core		
	LS model	YS model	Experimental results
l/h=10	5.6	5.8	5
l/h=50	4.03	4.41	3
l/h=90	0.87	1.37	1

core region. After consumption of the potential core of the jet, a sharp decay of maximum velocity is observed in the second region ($5 \leq x/h \leq 20$). In this region, the upper and lower shear layers of the jet start interacting and mix together. The flow stream starts spreading in the wall-normal and lateral directions. In the third region ($20 \leq x/h \leq 45$), velocity decay occurs according to the power law as described in equation 4.1.

Figure 4.13 shows the decay of u_{max} for the different initial conditions on account of nozzle length $l/h = 10, 50 \text{and} 90$. The initial velocity profiles created by these nozzles are developing velocity profiles in between the top hat and fully developed velocity profiles. The u_{max} remains constant in the potential core region. Table 4.2 shows the variation of potential core at different initial conditions. After consumption of the potential core, the u_{max} starts decaying as shown in figure 4.13. This region strongly exhibits the effect of initial conditions. In the last region, the decay rate of u_{max} is found independent of the nozzle length and the decay follows a power law, as described in the previous studies [9, 11, 13, 14]. The decay rate of u_{max} for the different initial conditions is listed in table 4.3. The smaller nozzle length produces a relatively higher value of the local maximum streamwise velocity (u_{max}) inside the flow domain. This is due to the uniform velocity

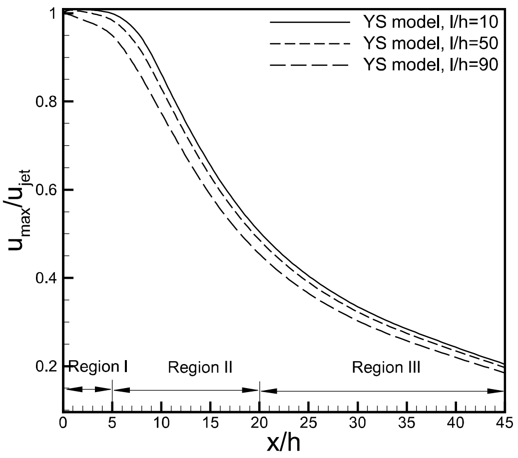

(a)

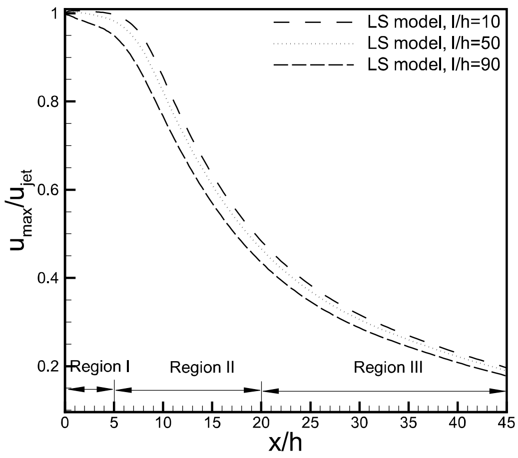

(b)

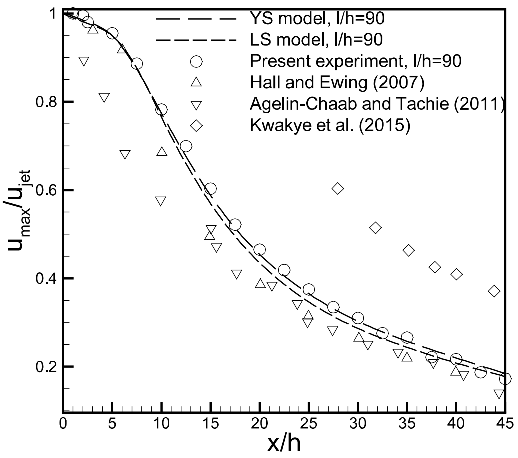

(c)

Figure 4.13: Decay of maximum streamwise velocity for the nozzle l/h=10, l/h=50, and l/h=90 for (a) YS model (b) LS model and (c) Comparison with present experiment for nozzle l/h=90, Hall and Ewing [9], Agelin-Chaab and Tachie [11] and Kwakye et al. [13]

Table 4.3: Decay rate of maximum streamwise velocity

Authors	Reynolds number	Decay Rate (n)		
		YS model	LS model	Exp.
Present case ($l/h = 10-90$)	25,000	1.06 ± 0.01	1.07 ± 0.01	1.08 ± 0.01
Hall and Ewing($l/h = 96$) [9]	89,600	-	-	1.144
Agelin-Chaab and Tachie [11]	5,000, 10,000, 20,000	-	-	1.15
Kwakye et al. [13]	12,000	-	-	0.996

profile at the jet exit.

In figure 4.13, numerical results of the decay of u_{max} are compared with the experimental results. The numerical simulations of LS and YS models predict results similar to the experimental results. The present study shows that the YS model accurately predicts up to the downstream locations $x/h \leq 35$. In contrast, after the downstream location $x/h = 35$, the LS model predicts more accurately than the YS model. The maximum deviation between experimental and numerical results of LS and YS models is approximately 7.6% and 7.8% respectively. The assumption of Boussinesq approximation might be the reason for the deviation of the numerical results. The decay of u_{max} of Hall and Ewing [9], Agelin-Chaab and Tachie [11], and Kwakye et al. [13] is compared with the l/h=90 nozzle. The deviation of these results from the present result is due to the different initial conditions and boundary conditions used by different authors. Hall and Ewing [9] and Agelin-Chaab and Tachie [11] used fully developed velocity profiles. Kwakye et al. [13] used high aspect ratio of the rectangular nozzle, which reduces the decay of u_{max}.

4.2.2 Variation of y_{max}/h

The variation of y_{max}/h along the downstream location (x/h) is shown in figure 4.14a. Here, y_{max}/h is defined as the non-dimensional locations of u_{max} from the bottom wall in the jet centerline plane. It also signifies the inner shear layer thickness that interacts with the bottom wall. From the figure 4.14a, it can be seen that y_{max}/h attains a minimum value after the consumption of the potential core, because of the interaction of the bottom wall with the inner shear layer and the spreading of the jet shear layers. The bottom wall restricts the spread and the bulk volume is accumulated over the bottom wall. As the fluid exits from the nozzle, entrainment in the upper shear layer occurs for all the cases. This causes y_{max}/h to shift towards the bottom wall from the jet centerline. It is also observed that due to the higher entrainment into the flow stream in the shorter nozzle, the u_{max} shifts towards the bottom wall as compared to the other nozzles. The linear variation of

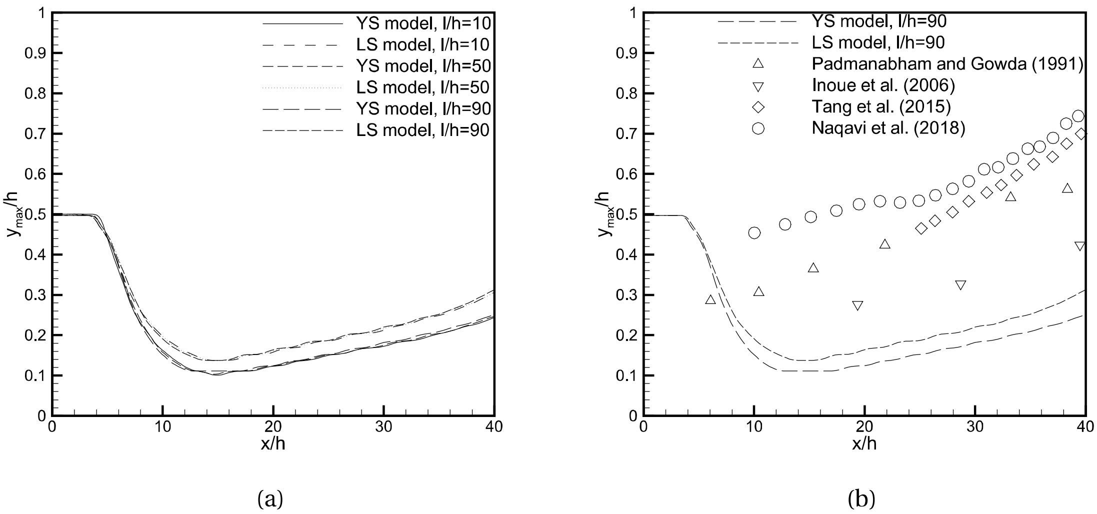

Figure 4.14: (a) Variation of y_{max}/h along the downstream direction (b) y_{max}/h comparison with Padmanabham and Gowda [2], Inoue et al. [10], Tang et al. [16] and Naqavi et al. [17]

Table 4.4: Comparison of y_{max}/h variation rate for nozzles $l/h = 10$, 50 and 90

	YS model		LS model	
	a	b	a	b
$l/h = 10$	0.007	-0.027	0.008	-0.023
$l/h = 50$	0.007	-0.026	0.008	-0.026
$l/h = 90$	0.007	-0.026	0.008	-0.024

y_{max}/h has been observed in the third region for all the nozzles. A linear equation is fitted as-

$$\frac{y_{max}}{h} = a\left(\frac{x}{h}\right) + b \tag{4.2}$$

The constant value of linear fit equation for different initial conditions is listed in table 4.4. The rate of variation of y_{max}/h is found independent of the initial conditions of the nozzle in far field locations ($x/h \geq 20$), as shown in table 4.4. Figure 4.14b shows the comparison of y_{max}/h variation for the nozzle $l/h = 90$ with the results of Padmanabham and Gowda [2] and Inoue et al. [10] in the far-field locations. They have found higher value of y_{max}/h as compared to the present case due to the higher jet exit velocity and mass flux. The y_{max}/h is also compared with the plane wall jet of Tang et al. [16] and Naqavi et al. [17]. They have found higher value of y_{max}/h due to the higher intensity of entrainment and two-dimensionalilty of the jet.

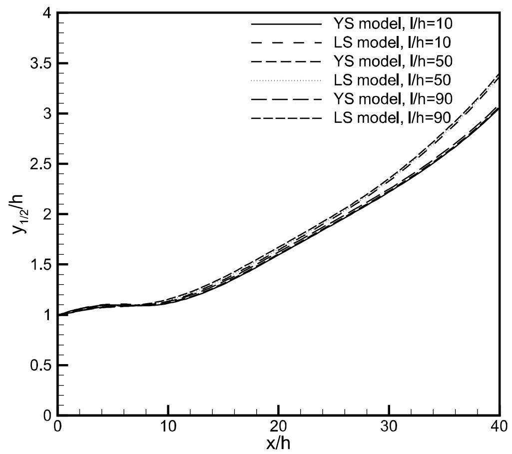

(a)

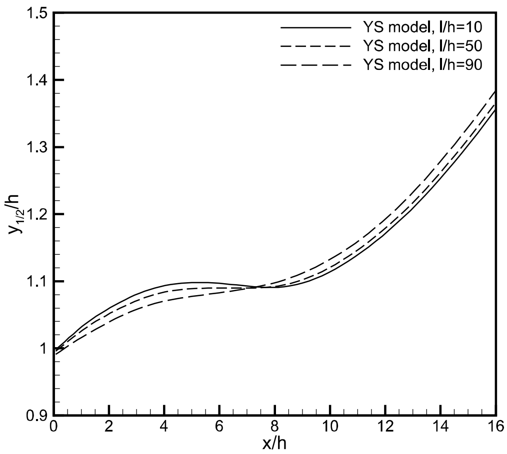

(b)

Figure 4.15: (a) Variation of jet half-width in wall-normal direction for YS and LS model (b) Zoom view of jet half-width in near field for YS model

4.2.3 Variation of jet half-widths

The spreading behavior of the wall jet in the downstream direction at different initial conditions has been numerically examined through the jet half-width. The jet half-width is defined as the location of streamwise velocity in the wall-normal and lateral directions, where $u = u_{max}/2$, u_{max} is the local maximum streamwise velocity. The variation of the wall-normal jet half-width with respect to the downstream locations (x/h) is shown in figure 4.15. From figure 4.15, it can be seen that the jet half-width decreases with increase in the nozzle length in the near field. This is due to the shape of the initial velocity profile at the jet exit. However, as the jet stream proceeds further downstream, trend of jet half-width gets reversed after $x/h = 7.3$ (YS model) and 7.6 (LS model). This is because of the high momentum for the shorter nozzle length, which pushes the bulk volume close to the jet centerline plane over the bottom wall. So, in the far field locations, the jet half-width decreases for the shorter nozzle length. In the far field locations ($x/h \geq 20$), the jet half-width varies linearly as

$$\frac{y_{1/2}}{h} = a\left(\frac{x}{h}\right) + b \tag{4.3}$$

The constant values of a and b are determined through the least square method and a is known as the spread rate $\left(\frac{dy_{1/2}/h}{dx/h}\right)$ of the flow stream. The spread rate in the wall-normal direction obtained through the YS and LS turbulence models, is shown in table 4.5. The

Table 4.5: Variation of jet spread rates in wall-normal direction

Authors	$\left(\frac{dy_{1/2}/h}{dx/h}\right)$
Present conditions,YS model (Nozzle $l/h = 10-90$)	0.060
Present conditions, LS model (Nozzle $l/h = 10-90$)	0.062
Present experiment (Nozzle $l/h = 10-90$)	0.056
Hall and Ewing [9]	0.05078
Agelin-Chaab and Tachie [11]	0.054

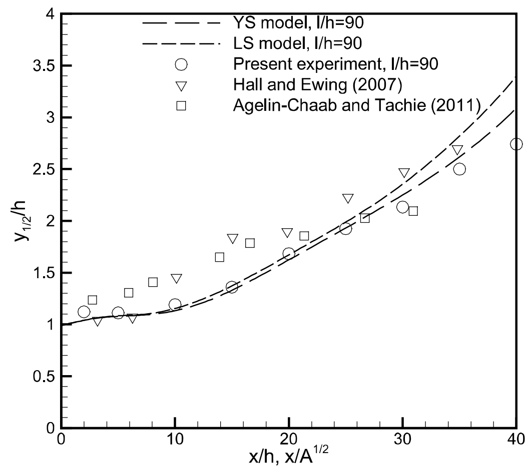

Figure 4.16: Comparison of jet half-width for nozzle $l/h = 90$ with Padmanabham and Gowda [2], Hall and Ewing [9], Inoue et al. [10] and Agelin-Chaab and Tachie [11]

spread rate is found independent of the nozzle length. The spread rate predicted by YS and LS models is approximately 7.1% and 10.7% higher than the present experimental results. The jet half-width is also compared with the results of Hall and Ewing [9] and Agelin-Chaab and Tachie [11] as shown in figure 4.16. Hall and Ewing [9] and Agelin-Chaab and Tachie [11] also proposed the linear profile similar to the present case. Agelin-Chaab and Tachie [11] considered a circular wall jet at the Reynolds number of 5,000, 10,000 and 15,000 while Hall and Ewing [9] have considered the rectangular wall jet with varying aspect ratios at a Reynolds number of 89,600. The above study considered a fully developed velocity profile with different nozzle geometries and found a lower spread rate than the present case.

The variation of the jet half-width in the lateral direction for the different initial conditions is shown in figure 4.17. From figure 4.17, it can be seen that the jet half-width varies linearly in the downstream locations after $x/h \geq 15$ and becomes independent of the ini-

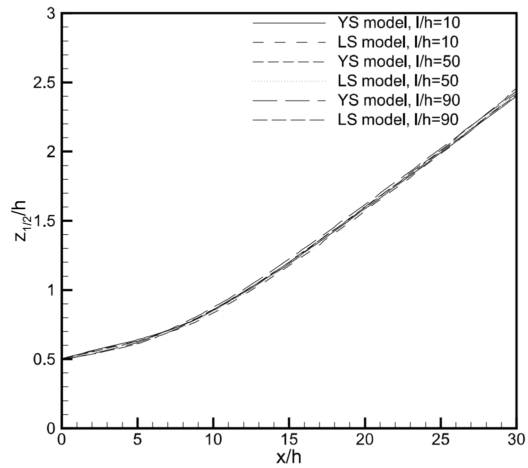

Figure 4.17: Variation of jet half-width in wall lateral direction

Table 4.6: Variation of jet spread rates in lateral direction

Authors	Constant value			
	a	b	c	d
Present conditions, YS model (Nozzle $l/h = 10-90$)	0.25	-3.25	-	-
Present conditions, LS model (Nozzle $l/h = 10-90$)	0.25	-3.27	-	-
Present experiment (Nozzle $l/h = 10-90$)	0.26	-3.54	-	-
Agelin-Chaab and Tachie [11]	0.255	-	-	-
Hall and Ewing [9]	0.0343	0.00663	0	5.48E-8

tial conditions. A linear equation along the downstream direction is included to define the spread rate as

$$\frac{z_{1/2}}{h} = a\left(\frac{x}{h}\right) + b \tag{4.4}$$

The constant values of a and b are listed in table 4.6. Hall and Ewing [9] defined the lateral spread with a fourth order polynomial for the different moderate aspect ratios of the nozzle, whereas Agelin-Chaab and Tachie [11] and present study considered a linear spread profile. The present numerical results are compared with the present experimental result of the nozzle $l/h = 90$, the results of Hall and Ewing [9] and Agelin-Chaab and Tachie [11], which are found in a good agreement with the numerical results with a little deviation due to the different initial and boundary conditions used. Both YS and LS models under predict the results from the experimental results in the far field locations due to anisotropic behavior of the sidewalls. The spread rate calculated by numerical models is approximately 3.8% higher than the experimental results.

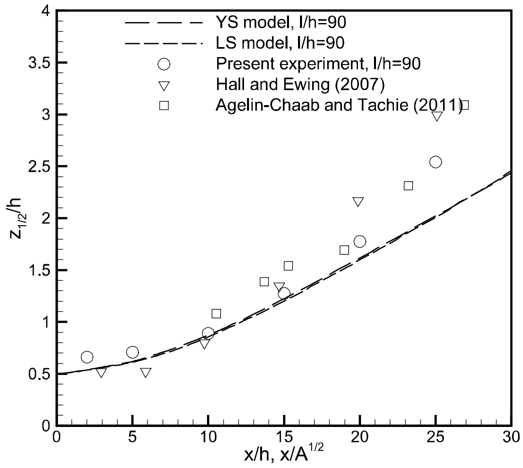

Figure 4.18: Comparison of jet half-width for nozzle l/h = 90 with Hall and Ewing [9] and Agelin-Chaab and Tachie [11]

4.2.4 Velocity and turbulent kinetic energy distribution

The effect of initial conditions on the flow field is examined through the velocity and turbulent kinetic energy contour plots. The velocity components u/u_{jet}, v/u_{jet}, w/u_{jet} and the turbulent kinetic energy $k_n = k/u_{jet}^2$ are plotted at x/h= 5, 15, 25 and 30. The negative values of v/u_{jet} contour represents the entrainment of the ambient fluid into the flow stream. The contours of velocity components and turbulent kinetic energy for nozzle l/h=10 and l/h=90 are shown in figure 4.19, 4.20, 4.21 and 4.22. Only contours of YS model are presented for different downstream locations. The effect of initial condition is clearly seen in figure 4.19a and 4.19b. The contours of nozzle l/h=10 have higher region of uniform velocity as compared to the nozzle l/h=90 around the jet center-line. The lateral and wall-normal spreads of u/u_{jet} contour are higher at this location for the nozzle l/h=10 as compared to the nozzle l/h=90 due to the shape of the initial velocity profile. The wall-normal and lateral velocity components (v/u_{jet} and w/u_{jet}) of the nozzle l/h=10 have highest value as compared to the other nozzles at x/h = 5. This phenomenon reflects the mixing among the shear layers. The strength of the lateral and normal velocity components is nearly 1.5% of the velocity component u/u_{jet} at this location x/h = 5. The turbulent kinetic energy is associated with the fluctuating velocity of the jet. For all the cases, turbulent kinetic energy is initially more in the upper and lateral shear layers as shown in figures 4.22a and 4.22b. The minimum turbulent kinetic energy is observed near y_{max}/h representing the low production of the fluctuating velocity. Further, at the downstream location x/h = 15, the strength of velocity component u/u_{jet} shifts towards

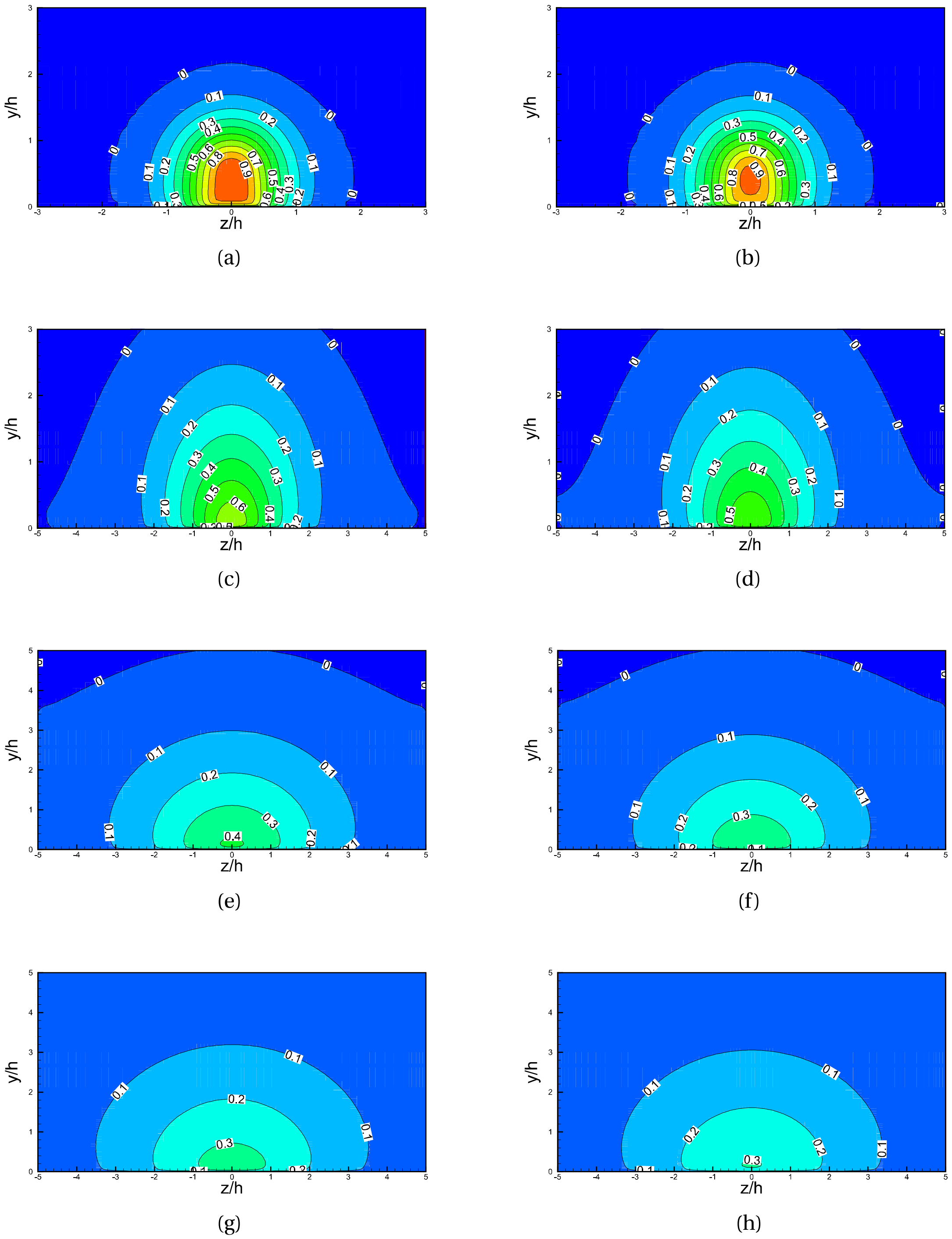

Figure 4.19: u/u_{jet} velocity contours at (a) $x/h = 5$ for $l/h = 10$, (b) $x/h = 5$ for $l/h = 90$, (c) $x/h = 15$ for $l/h = 10$ (d) $x/h = 15$ for $l/h = 90$, (e) $x/h = 25$ for $l/h = 10$ (f) $x/h = 25$ for $l/h = 90$ (g) $x/h = 30$ for $l/h = 10$ and (h) $x/h = 30$ for $l/h = 90$

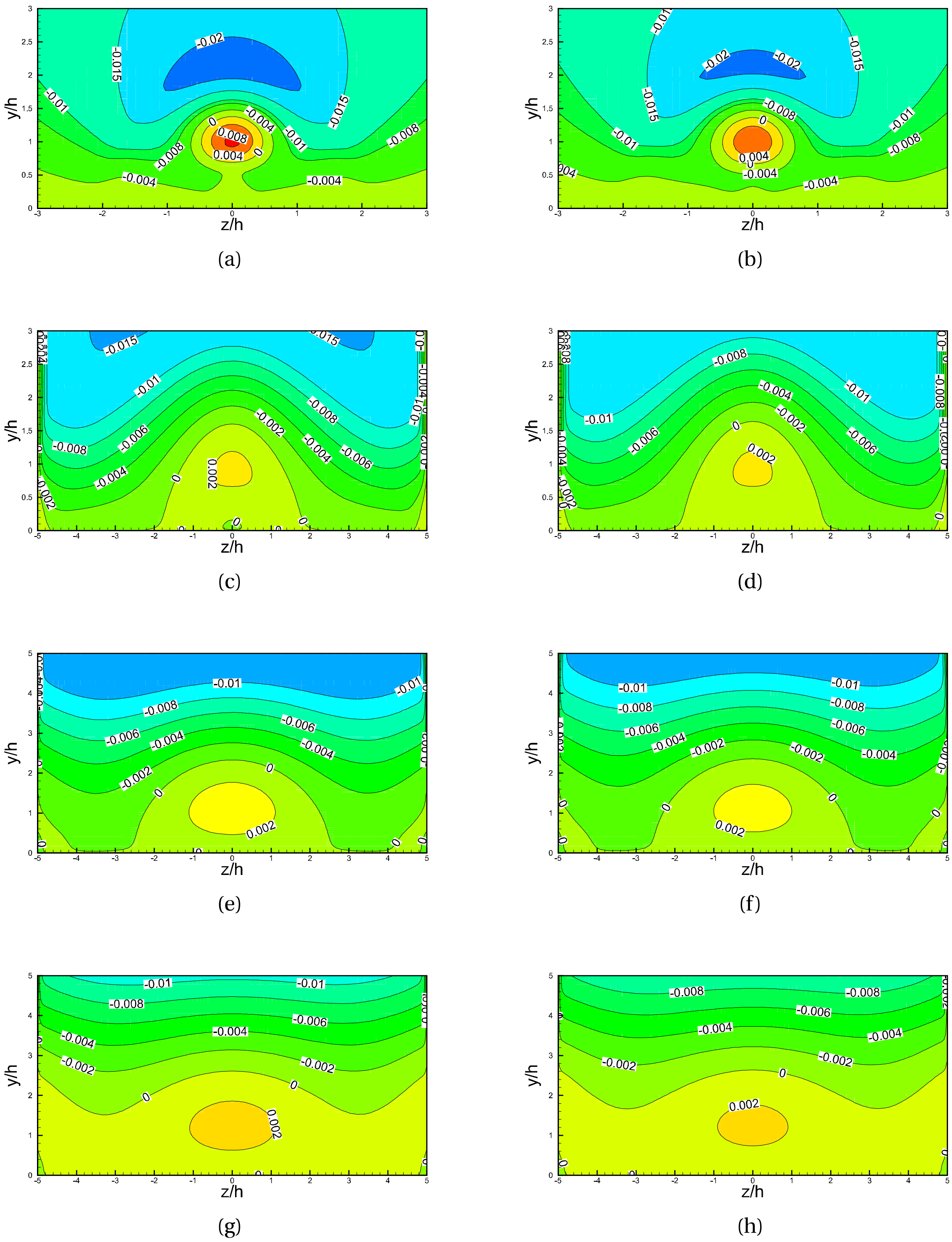

Figure 4.20: v/u_{jet} velocity contours at (a) $x/h = 5$ for $l/h = 10$, (b) $x/h = 5$ for $l/h = 90$, (c) $x/h = 15$ for $l/h = 10$ (d) $x/h = 15$ for $l/h = 90$, (e) $x/h = 25$ for $l/h = 10$ (f) $x/h = 25$ for $l/h = 90$ (g) $x/h = 30$ for $l/h = 10$ and (h) $x/h = 30$ for $l/h = 90$

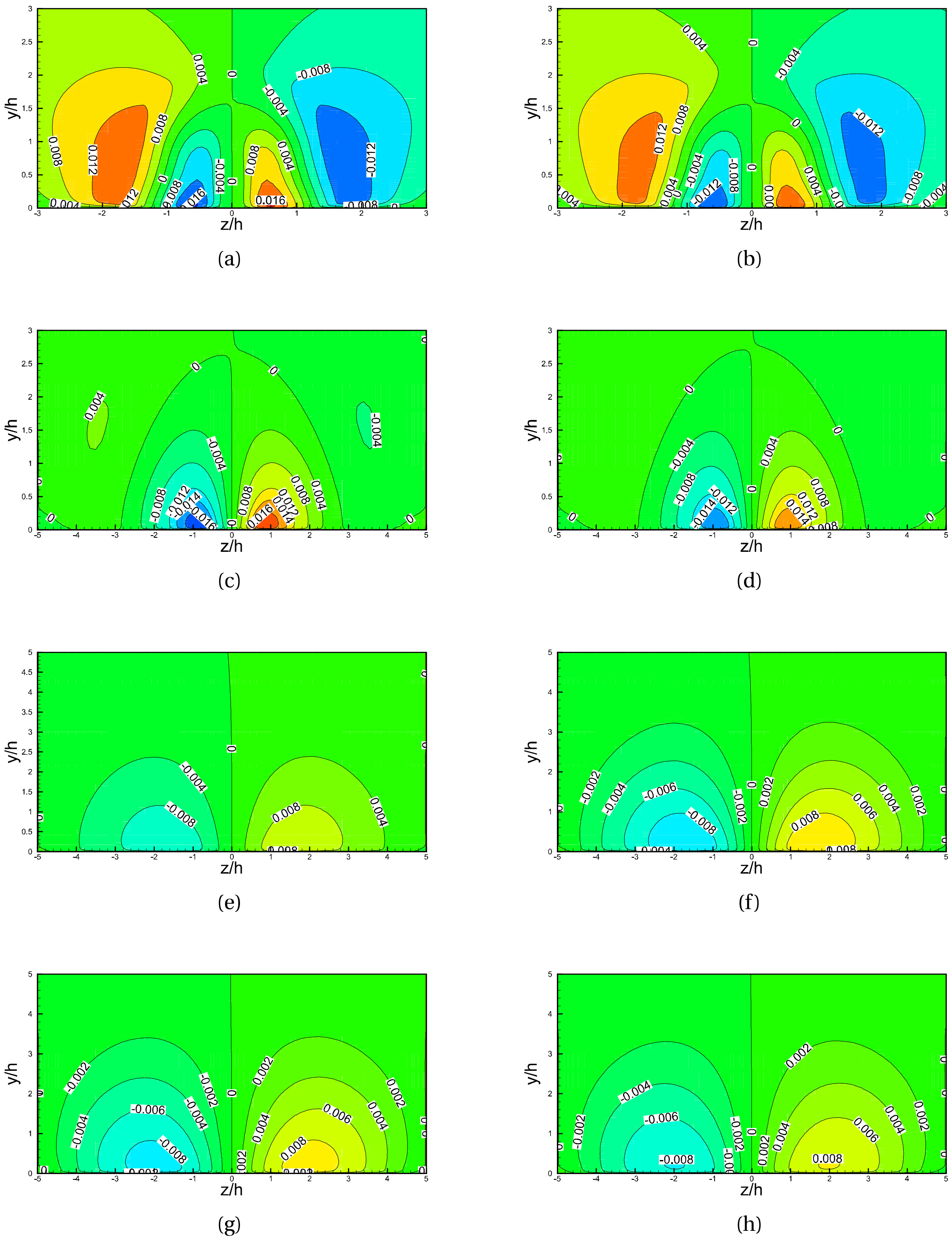

Figure 4.21: w/u_{jet} velocity contours at (a) $x/h = 5$ for $l/h = 10$, (b) $x/h = 5$ for $l/h = 90$, (c) $x/h = 15$ for $l/h = 10$ (d) $x/h = 15$ for $l/h = 90$, (e) $x/h = 25$ for $l/h = 10$ (f) $x/h = 25$ for $l/h = 90$ (g) $x/h = 30$ for $l/h = 10$ and (h) $x/h = 30$ for $l/h = 90$

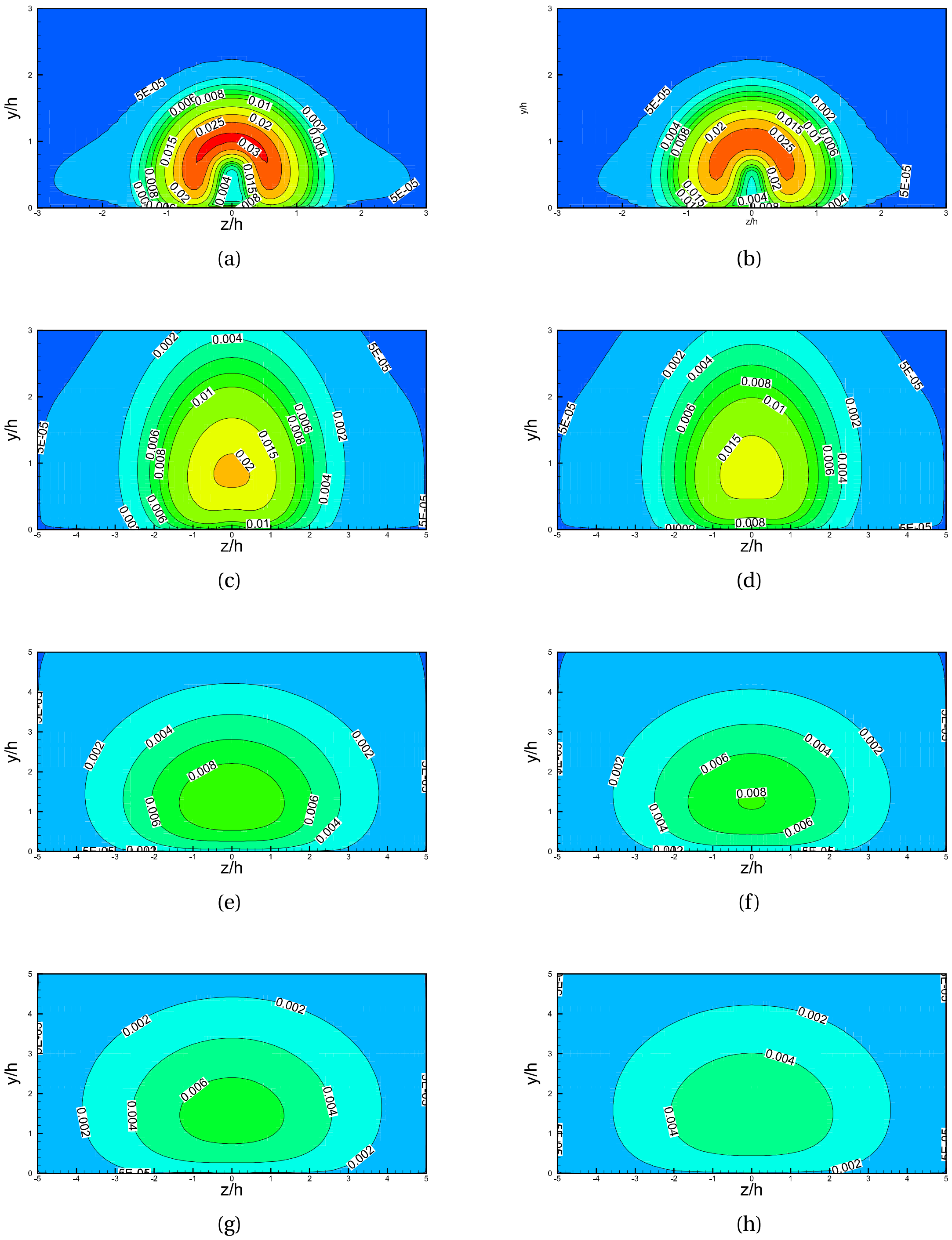

Figure 4.22: Turbulence kinetic energy $\left(k_n = k/u_{jet}^2\right)$ contours at (a) $x/h = 5$ for $l/h = 10$, (b) $x/h = 5$ for $l/h = 90$, (c) $x/h = 15$ for $l/h = 10$ (d) $x/h = 15$ for $l/h = 90$, (e) $x/h = 25$ for $l/h = 10$ (f) $x/h = 25$ for $l/h = 90$ (g) $x/h = 30$ for $l/h = 10$ and (h) $x/h = 30$ for $l/h = 90$

the bottom wall from the jet centerline $\left(z/h = 0.0 \text{ and } y/h = 0.5\right)$ due to suppression of the lower shear layer by the bottom wall and the ambient fluid. At x/h =15, the turbulent kinetic energy is higher in the upper shear layer as compared to the lateral and lower shear layers. This indicates that more turbulent structure and velocity fluctuation are present in the upper shear layer. This drives a secondary flow into the flow stream that leads to more growth in the wall-normal direction as compared to the lateral direction. Further, as the jet stream moves in the downstream direction $x/h \geq 25$, the turbulent kinetic energy diffuses into the flow stream and weakens at y_{max}. This leads to the minimization of the dynamic readjustment in the shear layers and the jet approaches self-similar behavior. The strength of lateral and wall-normal velocity components at $x/h = 30$ relatively increases and reaches up to 3% and 9% respectively of u/u_{jet} velocity component. These contours are quite similar to u velocity component contours, as reported by Hall and Ewing [9] for a square nozzle, and Sun and Ewing [4] for the circular nozzles. The sidewall restricted the spread in the lateral direction in the downstream locations ($x/h > 15$), and the climbing nature of the flow stream is observed adjacent to the sidewalls. Further in the downstream locations after $x/h > 30$ (not shown here), it is seen that the velocity of the flow stream adjacent to the sidewall is equal to the core velocity indicating a positive effect on the overall performance of the turbulent wall jet.

4.2.5 Similarity solution

The self-similarity is reached when the mean velocity profiles attain a congruence in wall-normal and lateral directions on a similarity scale. After attaining the self-similar profiles, no further relative readjustment takes place inside the flow field. Wygnanski et al. [32] suggested the similarity scale as the local mean velocity normalized by the local maximum streamwise velocity (u/u_{max}) and its location (y) normalized by the jet half width ($y_{1/2}$) as $y/y_{1/2}$. The self-similar profile for different initial conditions is shown in figure 4.23 in the wall-normal direction. Figure 4.23 denotes the velocity profile in the wall-normal direction, which indicates that self-similarity is achieved at x/h = 20 for l/h = 10 while conditions in other nozzles (l/h = 50 and 90) are still developing at x/h = 20. The delay in self-similar condition is due to the generation of different turbulent structures and entrainment of the ambient fluid into the flow stream, owing to the different initial conditions. The self similarity profile of Hall and Ewing [9] is shown in figure 4.24 for the comparison of the present numerical and experimental results of nozzle $l/h = 90$ at $x/h = 30$. The present numerical and experimental results show a good validity with [9].

The similarity profile for lateral direction is shown in figure 4.25. It is interesting to note that the effect of initial condition is not seen on the development of lateral self-similar be-

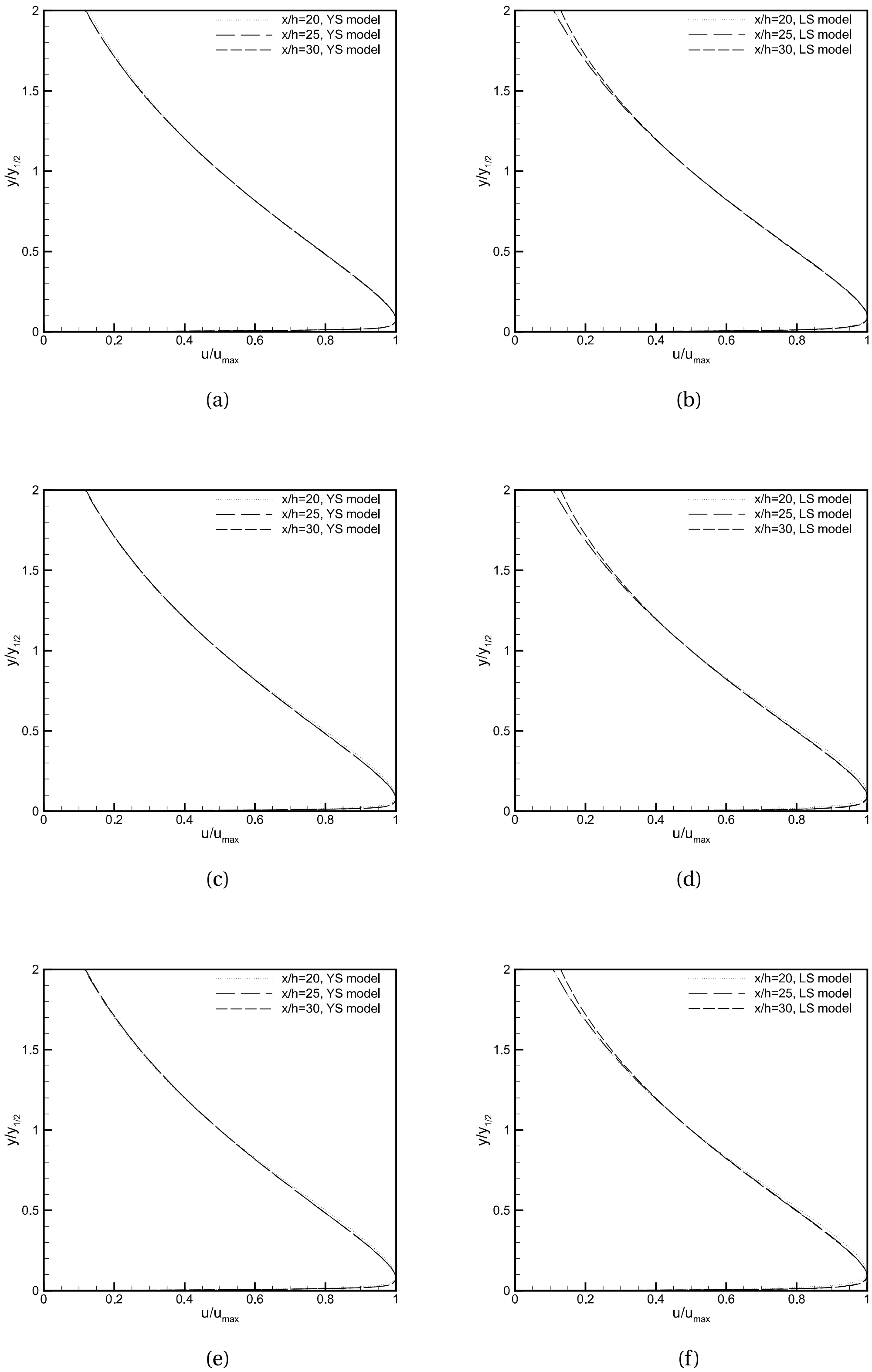

Figure 4.23: Self similar profile for Nozzle (a) YS model $l/h = 10$, (b) LS model $l/h = 10$, (c) YS model $l/h = 50$ (d) LS model $l/h = 50$ and (e) YS model $l/h = 90$ and (f) LS model $l/h = 90$

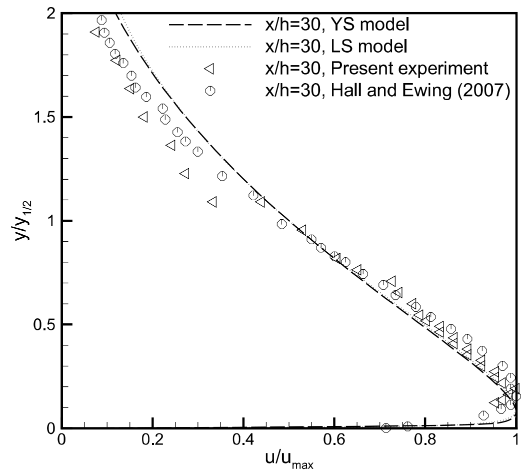

Figure 4.24: Self-similar profile comparison of YS and LS turbulence models for Nozzle $l/h = 90$ with present experiment and Hall and Ewing [9]

haviour. Also, the velocity profiles attain self similar solution earlier in the lateral direction as compared to the wall-normal direction. This indicates that more turbulent structure is present in wall-normal direction as compared to that in the lateral direction. This leads to destabilizing the wall-normal velocity profile and takes more time to get developed as compared to the lateral velocity profiles. The lateral similarity at $x/h = 30$ is also compared for nozzle $l/h = 90$ with the result of Hall and Ewing [9] and is found in a good agreement, as shown in figure 4.26.

4.2.6 Skin friction coefficient

The variation of skin friction coefficient $\left(C_{fw}\right)$ shows the drag force acting on the bottom wall. The skin friction coefficient for a wall jet can be calculated as $C_{fw} = \frac{\tau_{wall}}{\frac{1}{2}\rho u_{max}^2}$. Where, τ_{wall} is known as the wall shear stress, ρ is the density of the fluid (air) and u_{max} is known as the local maximum velocity along the downstream locations. The value of wall shear stress can be calculated from the expression $\tau_{wall} = \mu\left(\frac{d\bar{u}}{dy}\right)_{y=0}$, μ is the dynamic viscosity. The variation of the skin friction coefficient for the wall jet at different inlet conditions is shown in figure 4.27. From the figure, it can be seen that the skin friction coefficient decreases from a maximum value to a minimum value and then increases to a local maximum value in the potential core region (first region) for all the cases. This is because of the high velocity gradient present near the jet exit and near the bottom wall the turbulence in this region is $< u'v' >= 0$. After the consumption of the potential core, the coefficient of friction $\left(C_{fw}\right)$ starts decreasing for all the nozzles, due to intermixing of upper and lower

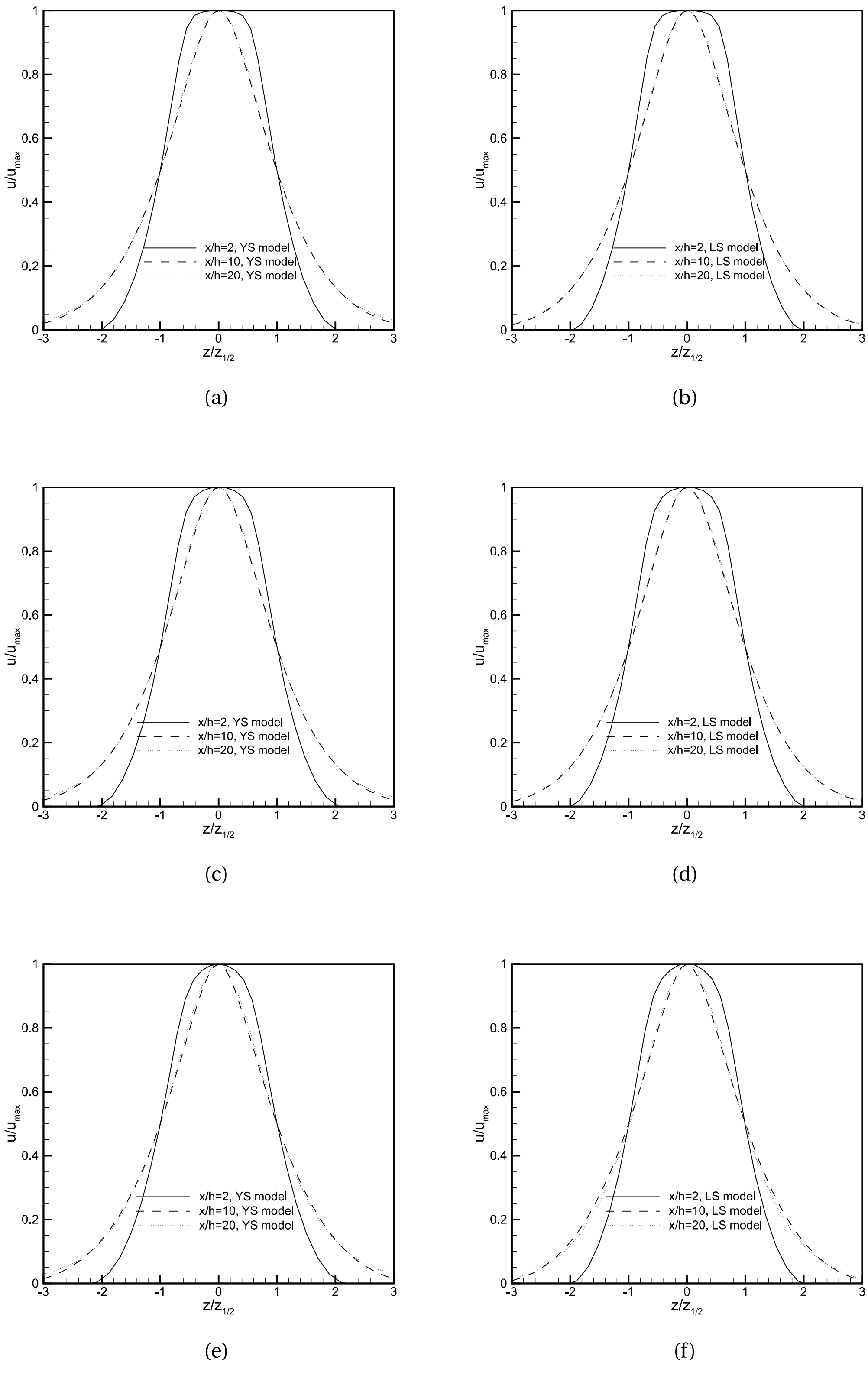

Figure 4.25: Self similar profile for Nozzle (a) YS model $l/h = 10$, (b) LS model $l/h = 10$, (c) YS model $l/h = 50$, (d) LS model $l/h = 50$ and (e) YS model $l/h = 90$ and (f) LS model $l/h = 90$

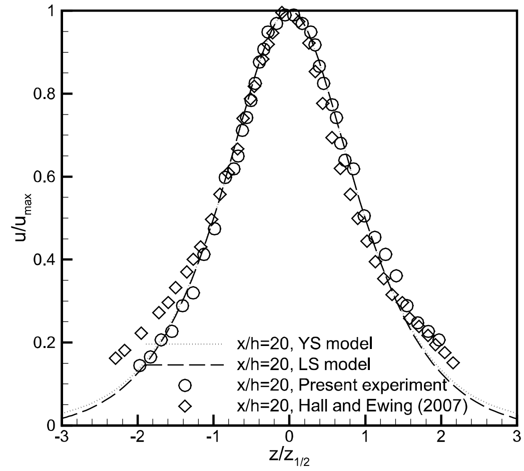

Figure 4.26: Self-similar profile comparison for Nozzle l/h = 90 with present experiment and Hall and Ewing [9]

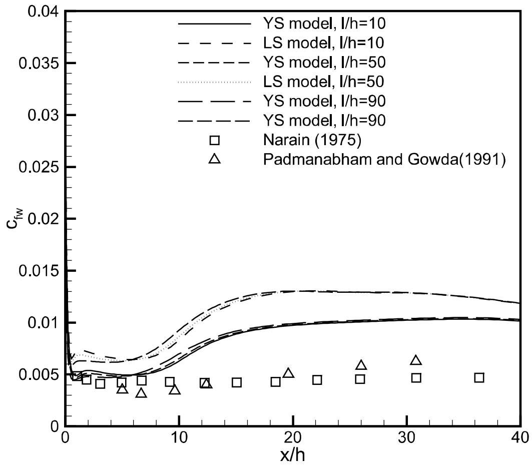

Figure 4.27: Variation of skin friction coefficient for different jet inlet conditions

shear layers and the decay of skin friction increases with decrease in the nozzle length. This is because different jet exit velocity profiles produce different turbulence structures between the flowing shear layers. In the far field locations, the skin friction coefficient is found independent of the initial conditions and it becomes constant for all the cases, as shown in figure 4.27. The measurement of skin friction coefficient in a three dimensional wall jet is very scarce. The results of the present case (square nozzle) is compared with the results of Narian [21] (rectangular nozzle) and Padmanabham and Gowda [2] (circular nozzle). The skin friction coefficient in the present case is found higher than the other results. The difference in nozzle geometry and jet exit Reynolds number are the reasons for the variation in the skin friction coefficient. The sidewall conditions of the present case also enhances the skin friction coefficient as compared to the aforementioned literature. The variation of C_{fw} with the Reynolds number is expressed as the power law $C_{fw} = K.Re_{max}^{-N}$. Where K is the proportionality constant, and $Re_{max} = u_{max} \cdot y_{max}/\nu$. The values of K and N are found to be 0.0315 and 0.169 respectively. The value of K and N falls within the range of reported values in the literature.

4.2.7 Reynolds shear stresses

The Reynolds shear stress reflects the mixing characteristics of the turbulent jet. So, Reynolds shear stress is a very important characteristic to characterize the turbulent wall jet. The Reynolds shear stresses are calculated (Biswas [133]) using the Boussinesq approximation as, $< u'_i u'_j > = (u'_i u'_j)/u_b^2 = -\frac{\vartheta_n}{Re}\left(\frac{\partial \overline{u_i}}{\partial (x/h)_j} + \frac{\partial \overline{u_j}}{\partial (x/h)_i}\right) + \frac{2}{3}k_n$. The normalized shear stress distributions of $< u'v' >$, $< u'w' >$ and $< v'w' >$ in the wall-normal direction at $x/h = 5$, 15, 25, and 40 are shown in figure 4.28. It can be seen from the figures 4.19a and 4.19b that the velocity gradient $du/dy > 0$ dominates in the lower shear layer at $x/h = 5$. So, a negative momentum of fluctuating velocity $\overline{v'}$ blows the fluid away from the jet stream and as a result, the stream-wise fluctuating velocity component $\overline{u'}$ increases ($\overline{u'} > 0$). Therefore, Reynolds shear stress term $< u'v' >$ attains a negative value and as it moves towards the location y_{max}/h. The fluctuating components start diminishing and $< u'v' >$ crosses 0 before the y_{max}/h (see figure 4.28a). Further, in the upper shear layer, the velocity gradient $du/dy < 0$; a positive momentum of the fluctuating velocity $\overline{v'}$ spreads the fluid in the wall-normal direction resulting in the increase in stream-wise velocity fluctuation $\overline{u'}$. This makes the Reynolds shear stress $< u'v' > > 0$ in the upper shear layer region and reaches up to a maximum value at $y/h = 1.021$ (for nozzle l/h =10, YS model). After reaching the maximum value, it starts decreasing due to the decrease in u/u_{jet} velocity in the upper shear layer. The Reynolds shear stresses $< u'w' >$and $< v'w' >$ are much smaller than $< u'v' >$ at this location. This is because of the negligible production of the fluctuating

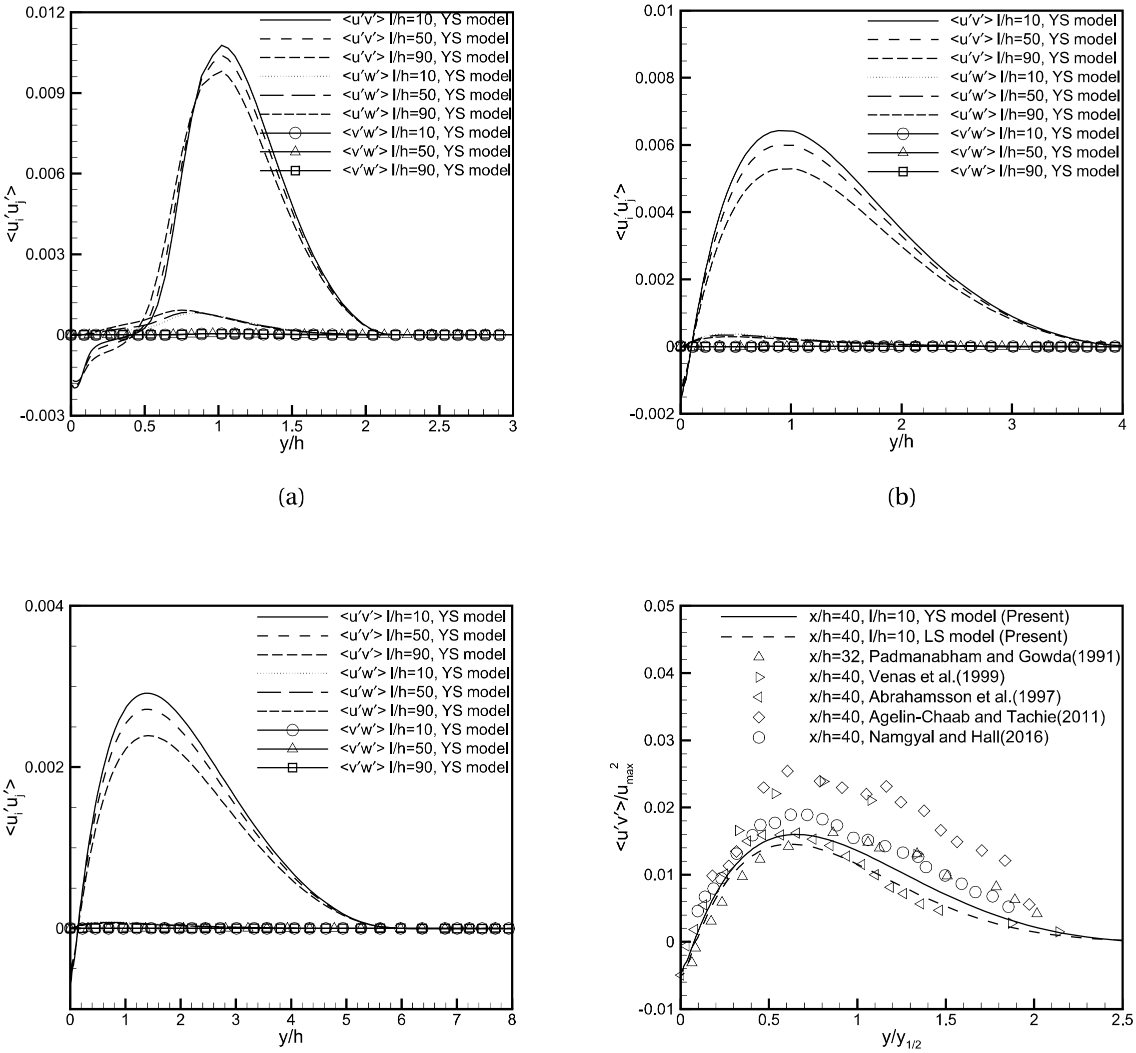

(a) (b) (c) (d)

Figure 4.28: Reynolds shear stress in wall-normal direction at symmetry plane (a) $x/h = 5$ YS model, (b) $x/h = 15$ YS model, (c) $x/h = 25$ YS model, (d) Comparison of Reynolds shear stress $< u'v' > / u_{max}^2$ at $x/h = 40$ for nozzle l/h=10

velocity $\overline{w'}$. The similar pattern of Reynolds shear stress $< u'v' >$ is observed by Padmanabham and Gowda [3], Sun [139], Namgyal and Hall [23] around the lower and upper shear layers. Further in the downstream location $x/h \geq 15$, the negative value of $< u'v' >$ in the lower shear layer starts shifting towards the wall (see figure 4.28b and 4.28c) because of the decrease in the velocity gradient du/dy and location of y_{max} too. Namgyal and Hall [23] did the experimental analysis of a three-dimensional turbulent wall jet using PIV method and found no evidence of this negative value of $< u'v' >$ after $x/h \geq 30$, but the present analysis shows the presence of negative value of $< u'v' >$. The possible reason might be the presence of this value very close to the wall which PIV did not account. In the upper shear layer, flow stream deforms continuously from the jet exit. This leads to a decrease in the momentum of the fluid in the downstream direction so that the positive fluctuation of v' spreads the fluid more intensively. Figure 4.28 also presents the comparison of the Reynolds shear stresses for the different initial conditions of the nozzle (l/h =10, 50 and 90). From the figure 4.28, it can be seen that the nozzle l/h =10 shows higher value of the Reynolds shear stress as compared to the other nozzles in the vertical jet centerline plane. The Reynolds shear stress is also presented in self similar coordinate of $< u'v' > /u_{max}^2$ vs $y/y_{1/2}$ at $x/h = 40$ and is compared with the results of Padmanabham and Gowda [3], Venas et al. [140], Abrasamsson et al. [12], Agelin-Chaab and Tachie [11] and Namgyal and Hall [23] in figure 4.28d. The present results show reasonably good match with the available literature results.

The Reynolds shear stresses ($< u'v' >$, $< u'w' >$ and $< v'w' >$) in the lateral direction at y_{max}/h are calculated and are shown in figure 4.29 for the downstream locations of $x/h = 5, 15, 25$ and 30. In the lateral shear layers the velocity gradient $du/dz < 0$. This suggests that the turbulent momentum of positive fluctuating velocity w' takes away the fluid from the jet axis, resulting in $u' > 0$ in this region. Therefore, Reynolds stress in the lateral shear layer $< u'w' > >0$ and attains a highest value in the lateral shear layer as compared to the other Reynolds shear stresses $< u'v' >$ and $< v'w' >$. Namgyal and Hall [23] also observed this behaviour of the Reynolds stresses at the downstream location $x/h = 5$ (see figure 4.29a). This may be due to the relatively larger convection in the lateral direction in three-dimensional turbulent wall jet. Further in the downstream locations $x/h \geq 15$, the Reynolds shear stress $< u'w' >$ dominates over $< u'v' >$ and $< v'w' >$ as shown in figures 4.29b and 4.29c. The figure 4.29 also compares the Reynolds shear stress generated by different initial conditions in the lateral directions at y_{max}/h plane. The figure 4.29 suggests that the dominated shear stress component $< u'w' >$ decreases with decrease in the nozzle length, up-to the downstream location $x/h = 5$;, whereas except this location, the trends got reversed. The Reynolds shear stress in the lateral direction is also compared

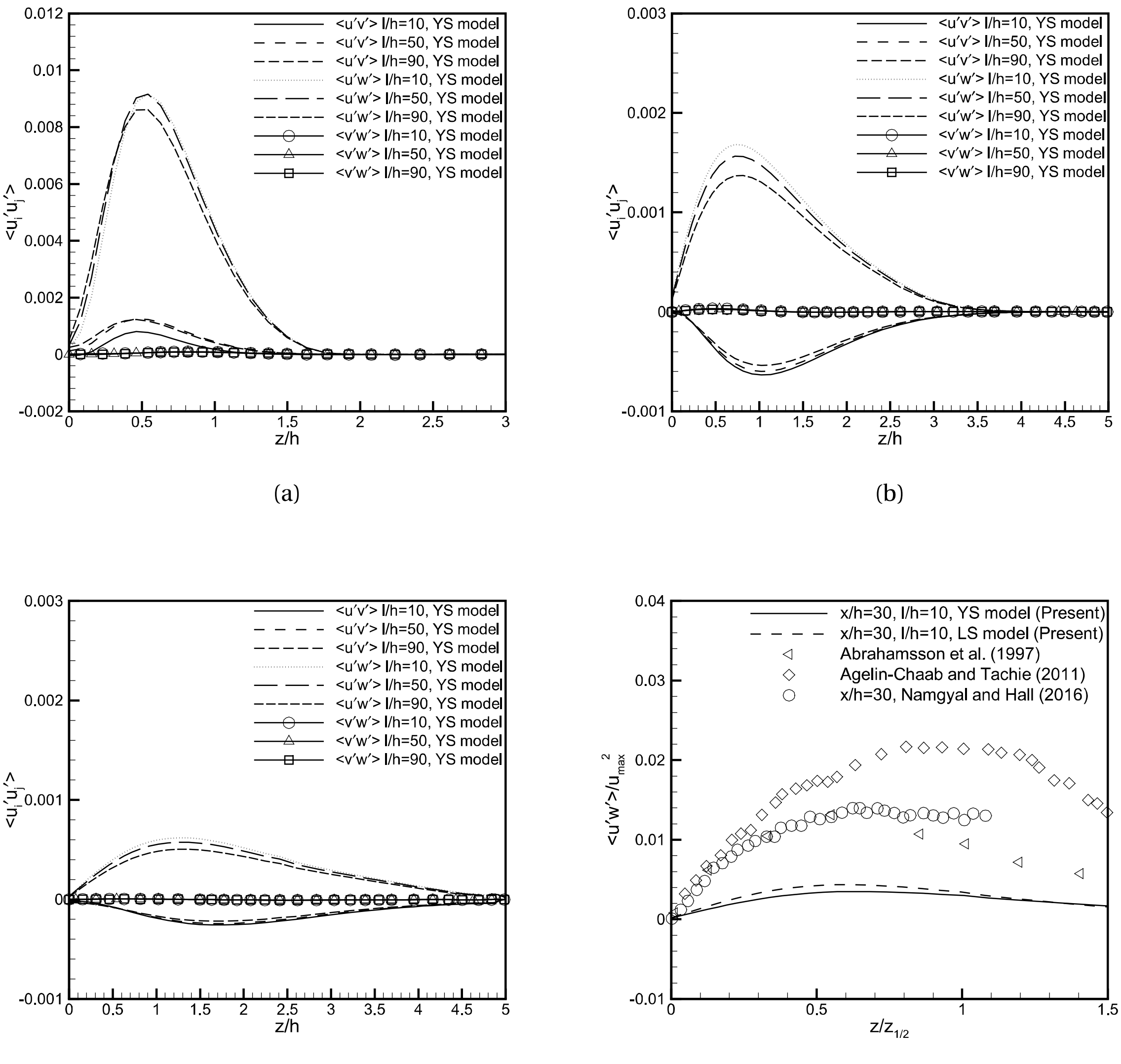

(a) (b) (c) (d)

Figure 4.29: Reynolds shear stress in lateral direction at symmetry plane (a) $x/h = 5$ YS model, (b) $x/h = 15$ YS model, (c) $x/h = 25$ YS model, (d) Comparison of Reynolds shear stress $< u'w' > /u_{max}^2$ at $x/h = 30$ for nozzle l/h=10

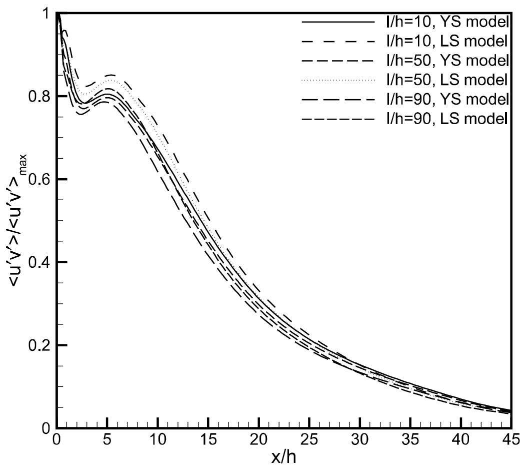

Figure 4.30: Maximum shear stress variation at symmetry plane

with the result of Abrahamsson et al. [12], Agelin-Chaab and Tachie [11] and Namgyal and Hall [23] on the similarity scale as $< u'w' > / u_{max}^2$ vs $z/z_{1/2}$ at the downstream locations $x/h = 30$ as shown in figure 4.29d. The maximum value of the Reynolds shear stress is lower in the present case due to the presence of sidewall, which causes reduction in the fluctuation of $\overline{w'}$ in the lateral direction as compared to Abrahamsson et al. [12], Agelin-Chaab and Tachie [11] and Namgyal and Hall [23].

The variation of maximum Reynolds shear stress $< u'v' >$ for the different initial conditions on symmetry plane is shown in figure 4.30. The Reynolds stress $< u'v' >$ is normalized by the maximum shear stress present on the symmetry plane as $< u'v' > / < u'v' >_{max}$. The Reynolds shear stress $< u'v' >$ gradually decreases as velocity dies down in the downstream direction for all the cases. From the figure 4.30, it can be seen that as the flow develops, the Reynolds shear stresses are reduced with increase in the length of the nozzle. It indicates higher mixing behavior of the shorter nozzle with the ambient fluid relative to the longer nozzle.

4.3 Conclusion

The effect of developing initial velocity profile conditions on three-dimensional turbulent wall jet is investigated through experimental and numerical methods. The mean flow characteristics are studied through experimental methods. The validation of the mean flow characteristics is done using the experimental results. In addition, the turbulent characteristics are studied through numerical methods. The initial conditions of the nozzle are varied by varying the nozzle length (l/h = 10, 50 and 90). The test section is made up of an acrylic sheet in which the sidewall is present at a distance of ± 100mm from the jet centerline. The bulk mean velocity and Reynolds number at the jet exit for all the cases are $20.3 m/s$ and $25,000$, respectively. A single probe hot wire anemometer is employed to measure the streamwise mean velocity field in the lateral and wall-normal directions across the jet centerline plane in the range of $0.2 \leq x/h \leq 50$. The numerical method has been carried out with the low Reynolds number $k-\varepsilon$ turbulence models suggested by Yang and Shih [47] and Launder and Sharma [48].

- The conclusion drawn through the experimental methods are as follows: The half-width is dependent on the initial conditions. In the near field, the wall-normal half-width is found higher for the nozzle length l/h=10 as compared to the nozzle length l/h=50 and l/h=90, whereas this trend is changed after x/h = 10. The spread rates of the jet half-widths in wall-normal and lateral directions are approximately independent of the nozzle initial velocity profiles. The present spread rates (0.056 and 0.26 in wall-normal and lateral directions respectively) are found within the range of the reported values in the literature. The decay of maximum mean velocity exhibits the dependency on the initial condition up-to x/h = 25. Beyond the $x/h \geq 25$, the decay rate of maximum mean velocity occurs as per the power law, and it is found independent of the nozzle initial conditions. The decay rates for maximum mean velocity after $x/h \geq 25$ are 1.08. The local Reynolds number variation is also estimated along the downstream directions and it is found that the local Reynolds number reaches approximately 56% of the jet exit Reynolds number at x/h = 40 for the nozzle l/h=10, whereas the other nozzles l/h=50 and l/h=90 have approximately $0.03Re$ and $0.02Re$ larger value than the nozzle l/h=10 at the same location. The mean velocity profiles become self-similar in the wall-normal direction at x/h = 20 for the nozzle l/h=10 while the other nozzles attain it at a larger downstream location (x/h = 25). The lateral similarity of the wall jet shows insignificant effect of the nozzle length. The delay in self-similar profiles in the wall-normal direction as compared to the lateral direction suggests that the more turbulence vortices are present in the upper shear layer as compared to the lateral shear layers. The agreement of the present similarity results with the results of other authors (in lateral and wall-normal directions) shows that self similar profiles are independent of the initial conditions of the nozzle. It is noted that the sidewall plays a significant role in deciding the fluid flow characteristics. As a result, the flow velocity near the sidewall becomes comparable to the core velocity after the attachment of the jet to the sidewall.

- The conclusion drawn from the numerical methods are as follows: The development of the three-dimensional wall jet shows dependency on the initial velocity profile in the near field ($x/h \leq 20$). The decay rate of maximum streamwise velocity in the far-field locations ($x/h > 20$) is found independent of the initial conditions, however local maximum streamwise velocity decreases with increase in the nozzle length inside the sidewall enclosure. The contours of velocity component suggest that the wall jet with nozzle length $l/h = 10$ has higher lateral (w) and wall-normal (v) velocity components compared to the other nozzles. This suggests intermixing among the shear layers, which increases with decrease in the nozzle length. The contours of turbulent kinetic energy exhibit the effect of the initial conditions in the near field. The spread rates in the wall-normal and lateral directions are found independent of the initial conditions, whereas jet half-width in the wall-normal direction increases with increase in the nozzle length. The mean velocity profile in wall-normal direction becomes similar at $x/h = 20$ for the nozzle $l/h = 10$, whereas for all the other nozzles, it gets a little delayed ($x/h = 25$). The lateral similarity of the wall jet shows insignificant effect of the nozzle length and shows similarity at $x/h = 10$ for all the nozzles. The skin friction coefficient shows the dependency on the initial conditions in near-field of the wall jet, whereas in far-field, skin friction coefficient attains nearly a constant value. The Reynolds shear stress $< u'v' >$ in the wall-normal direction is quite high as compared to the other Reynolds stresses, whereas, in the lateral direction, $< u'w' >$ dominates over the other Reynolds stresses. The Reynolds shear stresses decrease with increase in the nozzle length. It indicates higher mixing behavior of the shorter nozzle with the ambient fluid relative to the longer nozzle. It is noticed that the sidewall plays an important role in assessing the turbulent properties of the fluid flow. As a result, after the jet's reattachment to the sidewalls, the flow velocity near the sidewall is equal to the core velocity indicating a positive effect on the overall performance of the turbulent wall jet.